The Astrophysical Journal, 833:184 (24pp), 2016 December 20 doi:10.3847/1538-4357/833/2/184

OBSERVING THE FORMATION OF FLARE-DRIVEN CORONAL RAIN

E. Scullion[1,2], L. Rouppe van der Voort[1], P. Antolin[3], S. Wedemeyer[1], G. Vissers[1], E. P. Kontar[4], and P. T. Gallagher[2]
[1] Institute of Theoretical Astrophysics, University of Oslo, P.O. Box 1029, Blindern, NO-0315 Oslo, Norway; eamon.scullion@northumbria.ac.uk
[2] Trinity College Dublin, College Green, Dublin 2, Ireland
[3] National Astronomical Observatory of Japan, 2-21-1 Osawa, Mitaka, Tokyo 181-8588, Japan
[4] SUPA School of Physics and Astronomy, University of Glasgow, G12 8QQ, UK
Received 2016 January 23; revised 2016 September 17; accepted 2016 September 28; published 2016 December 16

ABSTRACT

Flare-driven coronal rain can manifest from rapidly cooled plasma condensations near coronal loop tops in thermally unstable postflare arcades. We detect five phases that characterize the postflare decay: heating, evaporation, conductive cooling dominance for ~120 s, radiative/enthalpy cooling dominance for ~4700 s, and finally catastrophic cooling occurring within 35–124 s, leading to rain strands with a periodicity of 55–70 s. We find an excellent agreement between the observations and model predictions of the dominant cooling timescales and the onset of catastrophic cooling. At the rain-formation site, we detect comoving, multithermal rain clumps that undergo catastrophic cooling from ~1 MK to ~22,000 K. During catastrophic cooling, the plasma cools at a maximum rate of 22,700 K s^{-1} in multiple loop-top sources. We calculated the density of the extreme-ultraviolet (EUV) plasma from the differential emission measure of the multithermal source employing regularized inversion. Assuming a pressure balance, we estimate the density of the chromospheric component of rain to be $9.21 \times 10^{11} \pm 1.76 \times 10^{11}$ cm^{-3}, which is comparable with quiescent coronal rain densities. With up to eight parallel strands in the EUV loop cross section, we calculate the mass loss rate from the postflare arcade to be as much as $1.98 \times 10^{12} \pm 4.95 \times 10^{11}$ g s^{-1}. Finally, we reveal a close proximity between the model predictions of $10^{5.8}$ K and the observed properties between $10^{5.9}$ and $10^{6.2}$ K, which defines the temperature onset of catastrophic cooling. The close correspondence between the observations and numerical models suggests that indeed acoustic waves (with a sound travel time of 68 s) could play an important role in redistributing energy and sustaining the enthalpy-based radiative cooling.

Key words: methods: data analysis – methods: observational – techniques: image processing – techniques: spectroscopic – telescopes

1. INTRODUCTION

Coronal rain is a transient phenomenon within coronal loops and represents a key component of the mass cycling between the solar chromosphere and corona, and it occurs frequently in active regions (e.g., Kawaguchi 1970; Leroy 1972; Levine & Withbroe 1977; Schrijver 2001; O'Shea et al. 2007; Antolin & Rouppe van der Voort 2012; Fang et al. 2013; Ahn et al. 2014; Antolin et al. 2015, and see references therein). During its formation, coronal rain momentarily constitutes the finest-scale substructures of coronal loops, making it important to investigate with respect to understanding the heating of loops, the building blocks of the solar corona.

Many observational studies of active regions indicate a general tendency for cooling (Terzo et al. 2011; Viall & Klimchuk 2012; Froment et al. 2015, and references therein). Coronal rain flows within a sheath of hot coronal plasma, as intermittent, elongated, and cool (chromospheric) condensations, follow trajectories tracing magnetic arcades and with densities varying between 2×10^{10} and 2.5×10^{11} cm^{-3}. This results in a substantial mass loss per loop of $1–5 \times 10^{9}$ g s^{-1} (Antolin et al. 2015). As the loop-top plasma cools and condenses, narrow, elongated clumps form that have been observed to fall back to the lower solar atmosphere at speeds greater than ~40 km s^{-1}. A comprehensive, statistical analysis of the properties of quiescent coronal rain in Hα 656.28 nm line scans, using high-resolution ground-based observations, was completed by Antolin & Rouppe van der Voort (2012), who reported average widths and lengths of ~310 km and ~710 km, respectively. Furthermore, the average temperatures of the dark clumps appear below 7000 K, with an average falling speed of ~70 km s^{-1}. On the other hand, flare-driven coronal rain was reported with an apparent constant projected speed of 134 km s^{-1}, and the downward acceleration is generally no more than 80 m s^{-2} (Martínez Oliveros et al. 2014).

Active-region coronal rain is observed in many other visible and near-infrared (IR) and extreme-ultraviolet (EUV) channels, such as Ca II 854.2 nm and He II 30.4 nm, as well as multiple other transition region (TR) emission lines indicating its multithermal structure (Antolin et al. 2015). Such cooling progression throughout TR temperatures has previously been considered to explain EUV brightness variations (Foukal 1976; Schrijver 2001; O'Shea et al. 2007; Tripathi et al. 2009; Warren et al. 2011). Cooling has been shown to continue with delays of up to 103 s between adjacent, parallel propagating strands (Schrijver 2001).

In this present work, we distinguish between the many detailed studies of nonflaring, widespread, active-region coronal rain as a relatively weak form of mass condensation (with respect to mass loading and energy input), and, henceforth, we refer to that as quiescent coronal rain. In this study, we are interested in the relatively stronger (i.e., higher density and infrequent) flare-driven coronal rain, which is investigated to a much lesser extent, due to the infrequency of multi-instrumental studies at sufficiently high resolution and unpredictable flares.

There have been many studies aimed at understanding cooling processes in postflare loops (e.g., Moore & Datlowe 1975; Antiochos & Sturrock 1978; Doschek et al. 1983; Fisher et al. 1985; Cargill 1993; Feldman

et al. 2003; Bradshaw & Cargill 2005; Klimchuk 2006; Warren 2006; Warren & Winebarger 2007; Reale & Landi 2012; Reale et al. 2012, and references therein). Statistical analyses of the cross-sectional widths of flare-driven coronal rain strands, within postflare loops, have been reported down to the diffraction limit of the most advanced ground-based instruments, with strong implications that rain strands may exist at even narrower widths (Scullion et al. 2014). Observational correspondences of redshifted plasma emission (downflow) after a flare, which was initially heated and blueshifted (upflow) to fill the postflare arcade loop system via chromospheric evaporation, have been widely reported (e.g., Brosius 2003; Raftery et al. 2008; Martínez Oliveros et al. 2014).

During the formation of coronal rain, the evaporated plasma, arising during flare heating in the impulsive phase, is rapidly cooled via thermal instability below 1–2 MK. Physically, the formation of coronal rain is thought to result from a loop-top thermal instability mechanism (Parker 1953; Field 1965; Cargill & Bradshaw 2013) when radiative losses exceed heating input to the coronal loop system. The cooling becomes accelerated at a late stage in this process, known as catastrophic cooling, whereby overdense hot or warm loops deplete plasma toward their foot-points, with progressively faster radiative cooling rates within multithermal loop strands. Using model calculations of conductively and radiatively cooled flare plasma, Doschek et al. (1982) calculated downflow velocities of $50\,\mathrm{km\,s^{-1}}$, consistent with quiescent rain observations. Numerical simulations of quiescent coronal rain formation suggests that catastrophic cooling is generally short-lived and dependent upon the foot-point heating parameters, but it is expected to occur in less than 1 hr typically (Mendoza-Briceño et al. 2005; Antolin et al. 2010; Susino et al. 2010). In the flare-driven scenario, we expect substantially larger foot-point heating coupled with impulsive and intense chromospheric evaporation, leading to greater mass loading of postflare loop systems.

Currently very little is understood about the nature of coronal rain at the point of formation in flare arcades, with respect to the accurate density or temperature variations across multiple spectral channels or the temporal evolution of catastrophic cooling, leading to the chromospheric component of coronal rain. In this study, we reveal the multithermal and multi-stranded nature of flare-driven coronal rain at its source during its formation. We investigate the temporal evolution of the cooling curve of the postflare arcade at the loop-top source in order to better understand the catastrophic cooling process using temperature diagnostics from the X-ray sensor on board the *Geostationary Operational Environmental* Satellites (*GOES*), the *Solar Dynamics Observatory*/Atmospheric Imaging Assembly (*SDO*/AIA; Lemen et al. 2012), together with dynamics from Hα 656.3 nm and Ca II 854.2 nm spectral scans obtained via the CRisp Imaging Spectro-Polarimeter (CRISP; Scharmer et al. 2008), located at the Swedish 1 m Solar Telescope (*SST;* Scharmer et al. 2003a).

In Section 2, we briefly outline the data-reduction steps undertaken in this analysis of coordinated *GOES*, AIA, and CRISP observations. In Section 3, we present the results of our observations of flare-driven coronal rain and investigate the properties of the coronal rain source with CRISP. In Section 4, we present our differential emission measure (DEM) analysis using multiple spectral channels in AIA to investigate the cooling processes (density and temperature variations both spatially and temporally) at the loop top in the rain-formation region, in the EUV. Finally, in the discussion section, we investigate the radiative and conductive cooling timescales using a simplistic flare cooling model and discuss the implications of the DEM analysis, in the context of the combined observations of catastrophic cooling.

2. DATA REDUCTIONS

We incorporate observations across a broad temperature range, using combined imaging and spectra at the highest cadence and resolution (within the respective passbands), via the *GOES* (0.05–0.4 nm and 0.1–0.6 nm) soft X-ray light curves, AIA (EUV) imaging in multiple spectral channels (see Figure 2 for some of the spectral channels used in this study), and CRISP for imaging spectropolarimetry in the visible and near-IR channels.

CRISP is a fast wavelength tuning, spectral imaging polarimeter that includes a dual Fabry–Pérot interferometer and consists of a wide-band and two narrow-band cameras (transmitted and reflected), as described by Scharmer (2006). CRISP is especially suited for spectroscopic imaging of the chromosphere in the popular Hα 656.28 nm and Ca II 854.2 nm spectral lines. CRISP is equipped with three high-speed, low-noise CCD cameras that operate at a frame rate of 36 fps. The spectral sampling is such that the transmission FWHM of CRISP Hα is 6.6 pm, and the prefilter is 0.49 nm. In these observations, the CRISP field of view (FOV) (see Figure 1) was centered at $[-349'', -329'']$ in solar-x/y on 2012 July 1 in the middle of AR 11515, and the observation sequence occurred between 15:08 and 16:31 UT. The CRISP wide-band FOV is coaligned with *SDO*/AIA using the background image (i.e., of the 170.0 nm continuum) of Figure 1, as a reference in the first time frame. The resulting FOV after clipping away CCD edge effects is $55'' \times 55''$. The observation specifications consist of sequential spectral imaging at six wavelength points about the upper chromospheric Hα 656.28 nm line center ($+/-0.1032$ nm), followed by nine wavelength points about the lower chromospheric Ca II 854.2 nm line center ($+/-0.0495$ nm), followed by a full Stokes sampling (Stokes I, Q, U, and V) at one spectral position in the photospheric Fe I 630.2 nm line (-0.0048 nm), resulting in an effective cadence of 19 s (i.e., effectively a reduced cadence as a result of frame selection of the highest-quality images). The image quality of the time series data significantly benefited from the correction of atmospheric distortions by the *SST* adaptive optics system (Scharmer et al. 2003b). Postprocessing was applied to the data sets with the image restoration technique Multi-Object Multi-Frame Blind Deconvolution (MOMFBD; van Noort et al. 2005). Consequently, every image is close to the theoretical diffraction limit for the *SST* with respect to the observed wavelengths. The pixel size of the Hα images is $0\farcs0597$. We followed the standard procedures in the reduction pipeline for CRISP data (de la Cruz Rodríguez et al. 2015), which includes the post-MOMFBD correction for differential stretching as suggested by Henriques (2012). We explore the fully processed data sets with CRISPEX (CRISP-EXplorer) (Vissers & Rouppe van der Voort 2012), which is a versatile code for analysis of multidimensional spectral data cubes available through SolarSoft.

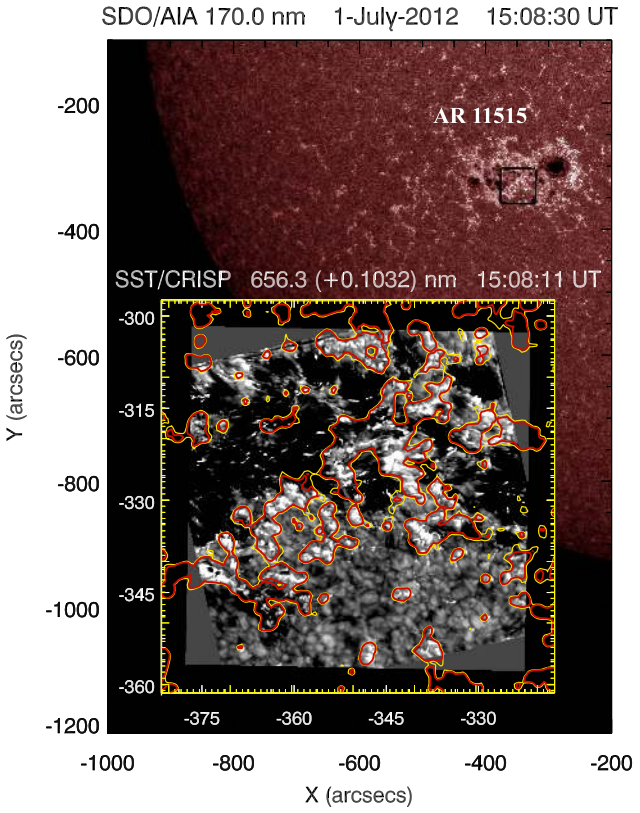

Figure 1. The *SST*/CRISP gray scale Hα 656.28 nm (+0.1032 nm) spectral image (inset) and the *SDO*/AIA 170.0 nm continuum perspective image (background) are presented for comparison. The CRISP FOV (white box overlaid on the continuum image) is centered on active region (AR) 11515 on 2012 July 1 at 15:08:30 UT. The 170.0 nm photospheric bright points are contoured over the CRISP Hα coincident images and used as a reference for the coalignment of the data sets in space and time.

The *GOES* X-ray observations are obtained using the *GOES* graphical user interface within the SolarSoft (SSWIDL) routines and processed for cleaning and background subtraction[5] (Ryan et al. 2012) of soft X-ray flux, temperature, and emission measure (EM) light curves (as presented in Figures 2 and 20 for the 0.05–0.4 nm passband). Similarly, AIA data are processed from level 1.0 to level 1.5 using standard SSWIDL routines to correct for dark and flat fielding, plate-scale corrections, and limb fitting for alignment between the AIA channels with 170.0 nm (a reference channel for coalignment). *SDO*/AIA observes with a cadence of 12 s and a pixel size of 0.″6 (corresponding to a spatial resolution of ∼1.″6). With the level 1.5 data product, it is expected that there is a small spatial offset between the internal AIA channels on the order of 0.25–0.5 AIA pixels (Aschwanden & Boerner 2011). To achieve sub-AIA pixel accuracy in the temporal and spatial coalignment of CRISP images with AIA, we cross-correlate the clearly identifiable active-region bright points. The AIA images are then derotated to that time frame, and the bright points are tracked in time, with CRISP enabling the excellent coalignment throughout the observation.

[5] We followed the TEBBS procedure for Temperature and Emission measure-Based Background Subtraction, outlined here: http://www.solarmonitor.org/tebbs/about/.

3. OBSERVATIONS OF FLARE-DRIVEN CORONAL RAIN

The C8.2-class solar flare impulsive phase lasted for 3 minutes 10 s according to the *GOES* light curve in the 0.05–0.4 nm channel for soft X-ray emission, as presented in Figure 2 (main panel). The postflare decay phase in X-ray emission lasted for 18 minutes after it reached a peak at 15:44:40 UT, then the EUV postflare arcade became visible in the hottest AIA channels, as is presented in Figure 2 (inset). During the formation of EUV postflare loops (i.e., between 16:05 UT and 16:23 UT), we detected a strong flow of multiple coronal rain strands in the chromospheric Hα line, which appears to fall back toward the surface within the EUV loop cross sections. We identify the origins of this flow to lie within the yellow box region of Figures 2 and 3. This region is the focus of further investigation in this study into the nature of coronal rain formation. The multiple, dark coronal rain strands are presented in Figure 3 (right panel). The left panel shows the wide-band image from the Fe I 630.2 nm spectral window, which represents the signal at the photospheric surface. It is clear that there is no white-light signal associated with the flare, which is common for weaker (C-class) flares. In Figure 3, we clearly demonstrate that the source and sink of flare-driven chromospheric plasma in coronal rain, and ultimately the origins of its existence, lies in the bright Hα ribbon formation (foot-point heating), visible within the red-wing images of Hα (middle panel). The time delay between the flare ribbon formation and the first appearance of coronal rain formation (frame no. 88, 16:10:19 UT) is ∼26 minutes, and by 16:15:06 UT we detect a full development of the rain strands farther along the loop leg, returning to the location of the ribbons. In order to investigate the properties of the formation of the return flow as coronal rain from the loop top, we use the Hα line core imaging, which reveals the structural details of the chromospheric plasma.

In Figure 4, we zoom into the yellow box region of the coronal rain source and present the Hα line core images (first row) for frame no. 89 (16:10:39 UT). This loop-top source is initially in emission in Hα and located with the green arrow. At 16:12:23 UT this bright source cools into an absorption profile and becomes more extended spatially (to the left and right of the loop top) by 16:13:57 UT, as it proceeds to fall back toward the foot-points. This bright source is very localized and initially has a circular cross section of ∼11,000 km^2 before becoming more elongated by 16:12:23 UT. By 16:13:57 UT, we can detect at least eight parallel, darker (cooler) strands at the loop top. When we consider the Doppler velocity of the Hα flow field at the source of the coronal rain (third row), we do not detect any net flows at the loop-top sources. Only along the path of the blue curve do we detect a strong net redshift of 12.0 $\pm$ 0.3 km s^{-1}, which corresponds to the location of the darkest rain strands in the far red wing of Hα (first row, third panel). The thermal velocity maps (fourth row) are determined from the Doppler broadening of the spectral scans per pixel. The method used to determine these velocities involved subtracting the background by using image frames from before and after the formation of the rain within the yellow box region. Then we determined a reference profile through averaging the spectral profiles per pixel in a small region away from the rain formation where there is no activity within the interval of the rain formation (i.e., from 16:05 UT to 16:23 UT). We then measured the Doppler shifts and FWHM per pixel in the rain

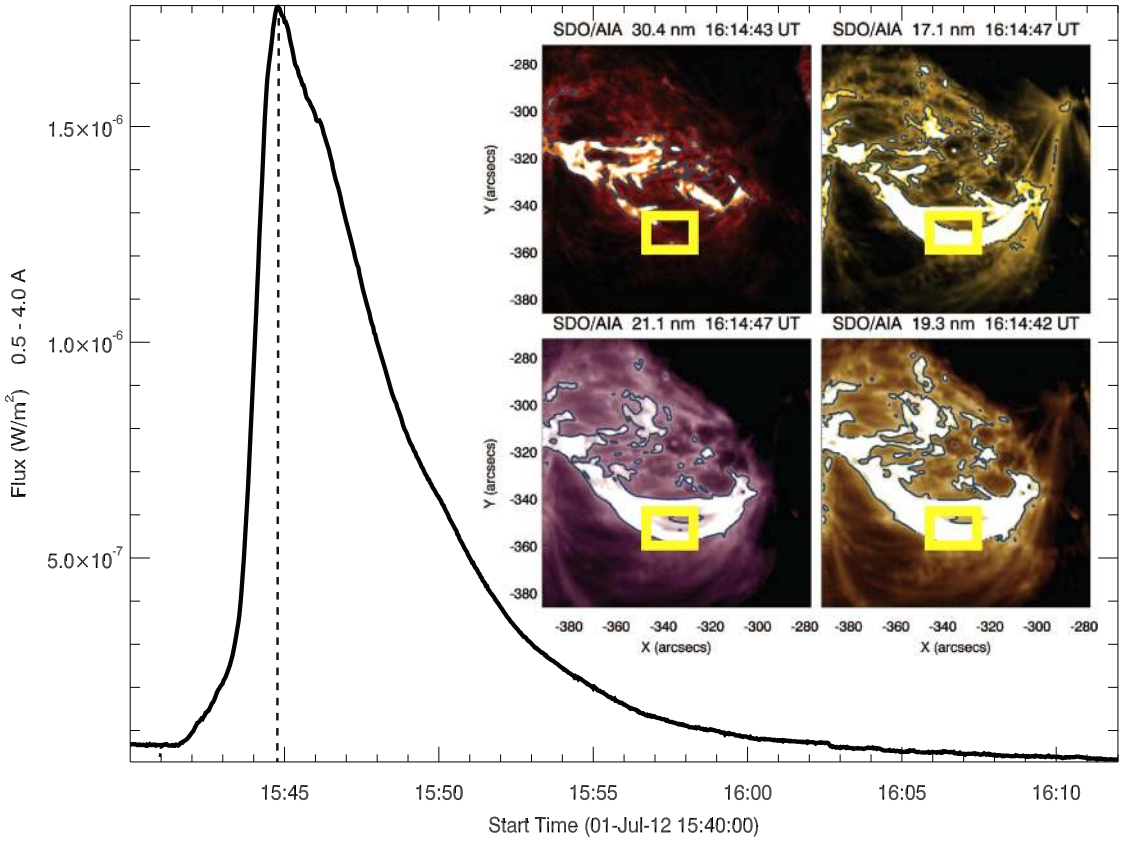

Figure 2. Main panel: the *GOES* 3 s X-ray flux (W m^{-2}) light curve, for the 0.05–0.4 nm passband, is presented in the time range from 15:40 UT to 16:12 UT, for the C8.2-class flare. The vertical dashed line marks the peak time (~15:44:40 UT) for the flare energy deposition. Inset: the AIA postflare EUV loops, as they appear 30 minutes after the *GOES* X-ray flux peak, are presented for He II 30.4 nm (top left), Fe IX 17.1 nm (top right), Fe XIV 21.1 nm (bottom left), and Fe XII 19.3 nm (bottom right). The yellow box marks the region of interest within the flaring loop cross section near the loop top of the flaring arcade and the focus of the remainder of the coronal rain formation study.

strands relative to the reference profile. The alternative method of fitting a Gaussian profile to the spectral profile in Hα is not so effective given the relatively low number of spectral positions scanned. There is a strong thermal broadening in the range of 4–12 $\pm$ 0.3 km s^{-1} at the location of the bright Hα loop-top sources of coronal rain (fourth row). We can estimate an upper limit for the corresponding gas temperature of the emitting region from the line-width broadening in the rain formation with

$$T = \frac{1}{8\ln 2}\frac{c^2 m_{\rm H}}{k_{\rm B}}\left(\frac{\rm FWHM}{\lambda_0}\right)^2, \quad (1)$$

where k_b is the Boltzmann constant, λ_0 is the rest wavelength of the reference profile, and $m_{\rm H}$ is the mass of a hydrogen atom, and here we ignore microturbulence physics. The resulting temperature map for the yellow box region of Figure 4 is presented in Figure 6. To determine the nonthermal speed from Figure 4, we used a rearrangement of Equation (1), and we assume that the Doppler width of the reference profile represents the quiet Sun formation temperature of the Hα line of 1 $\times$ 10^4 K.

In Figure 5, in a similar fashion as with Figure 4, we investigate the lower chromospheric Ca II 854.2 nm line core signatures of the loop-top rain formation within the yellow box region. We do not detect any signatures of redshifted dark coronal rain strands in Ca II 854.2 nm at the corresponding times. However, we detect a bright coronal rain source, marked with the green arrows, which are on average smaller in cross section and relatively less bright (with respect to its background) compared with the same Hα bright source (compared with its background level) for the same time frame. In the line core images we detect the faint signatures of absorption of rain strands at the loop top, extending away from the bright source, in the same locations as the dark strands from Hα. This implies that the temperature and density properties of coronal rain at the loop top may be much more structured at the loop top than along the loop leg. The detection of Ca II coronal rain source features implies that the plasma temperature must cool further, below Hα formation temperatures, in agreement with measurements of quiescent coronal rain in Antolin et al. (2015). We do not detect anything significant within the dopplergrams or line width broadening maps for Ca II because the signal in the rain is so weak on disk.

From Figure 6, we map the temperature distribution and find that the hottest components of the source of the rain, corresponding to the brightest structures, are at most 20,000–22,000 K. When we consider plasma at 14,000–16,000 K, we can detect the faint outline of the postflare loop arcade in the chromospheric plasma, which may indicate that the chromospheric plasma remains thermally confined to the magnetic structure of the loop system in partial ionization. As mentioned previously, the flow field in the Hα coronal rain is traced with a blue curve in Figure 3 (right panel). From this blue curve, we extract time–distance plots to learn more about the nature of the coronal rain flow field, as

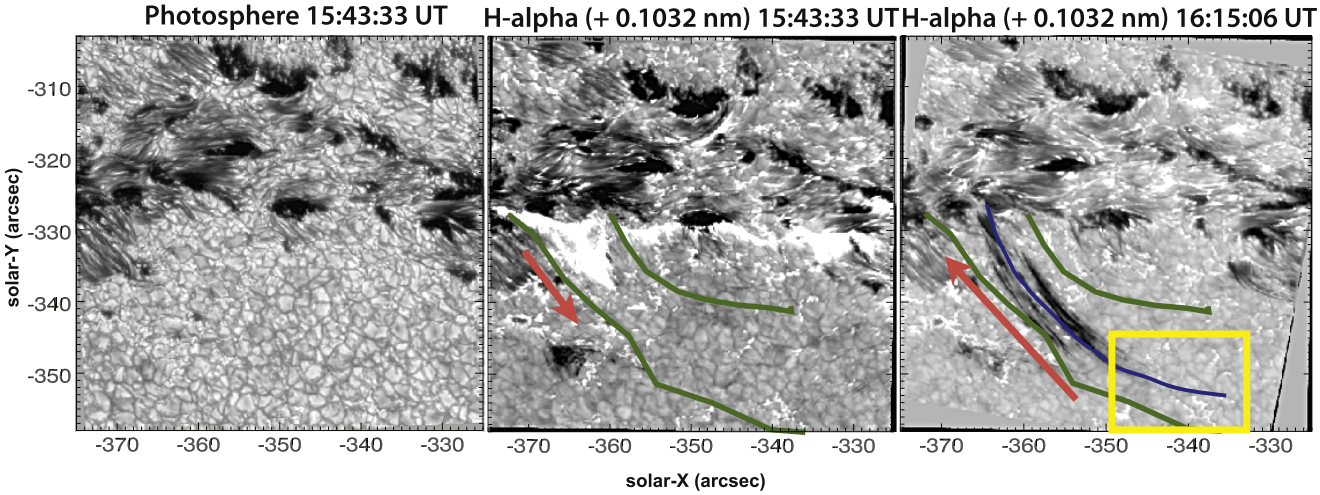

Figure 3. We observe the Hα spectral line at the far red-wing position (+0.1032 nm: middle and right panels at different times) during ribbon formation at 15:43:33 UT (middle panel at solar y: −330 arcsec) and later of the chromospheric component of coronal rain at 16:15:06 UT (right panel). We present the photospheric Fe I 630.2 nm channel wide-band image (left panel) at the time of chromospheric ribbon formation. We can spatially correlate the EUV postflare loop boundary (as presented in Figure 2) overplotted as a green contour (middle and right panels). The blue curve marks the loop-leg cross-cut (right panel) used to produce the time–distance diagrams shown in Figures 7 and 8. The arrows depict the direction of propagation of the left-most ribbon structure during the ribbon formation (middle panel) and the subsequent direction of the coronal rain flow from the loop-top source (right panel), which is within the yellow box.

presented in Figures 7 and 8. The one-to-one correspondence of these sources with the EUV loop activity will be discussed later in this section.

In Figure 7, we measure the flow-field properties of the coronal rain strands (beyond frame no. 86, marked by the vertical red dashed line: 16:09:44 UT), as they fall back toward the postflare foot-point within the Hα far red wing (+0.1032 nm) FOV. The loop half-length (L) is 32 $\pm$ 0.4 Mm and is traced by the blue curve cross-cut used to extract the time–distance plots. Note that the loop half-length was determined through measuring the separation of the foot-points of the postflare arcade, using the midpoint of the loop cross section as observed in the 17.1 nm channel from AIA, at the time of coronal rain formation in Hα (see the contoured loop arcade in 17.1 nm in the inset panel of Figure 2). This foot-point separation is measured as 56 arcsec. We then determined the loop half-length from a half circle assuming a circular postflare loop has formed between the foot-points. At frame no. 88, we detect the onset of redshifted, dark flows along the loop leg, which flow back to the foot-point. The bright flare ribbon exists at the foot-point until frame no. 40 and extends outward along the loop by ~4300 km, implying an outward propagation of this heating signature into the postflare loop system. The longest continuous coronal rain strands detected here are ~10,700 km, assuming we do not need to consider projection effects in this estimation. The rain strands appear to fall back within a range of velocities spanning 52–64 km s^{-1} and exhibit periodicity. We can detect 10 sequential strands (marked with arrows), which appear to last for typically three to four time frames (corresponding to 55–70 s) and are separated by a similar time interval. The rain shower (a term first coined by Antolin & Rouppe van der Voort (2012) describing a sudden onset of multiple rain strand formations) appears to end at frame no. 125 (16:22:38 UT), resulting in a shower lifetime in the range of 770–780 s.

In Figure 8, we consider three time–distance diagrams for the blue curve track derived from the image's different spectral positions in Hα. We detect the initial, bright coronal rain source that was also present in the FOV from Figure 4. At +0.1032 nm, the rain strand exists closer to the loop foot-point (50–200 on the y axis), whereas at +0.0774 nm the same strand is detected at an earlier time and closer to the loop top (120–300 on the y axis). Furthermore, the loop-top component of the rain can be detected in the Hα core between 200 and 360 and appears to originate as a bright source (within the yellow box) at frame no. 88. The coronal rain flow extending from this bright source (highlighted with the blue solid line) has an apparent velocity of 23.1 $\pm$ 2 km s^{-1}. In the subsequent panels, scanning farther into the red wing, we detect progressively faster flows (highlighted with purple and red solid lines) corresponding to 40.6 $\pm$ 2 km s^{-1} and 54.5 $\pm$ 2 km s^{-1}, respectively. The coronal rain flow overall appears to accelerate in time, from frame no. 88 (red vertical dashed line) at the loop top until it reaches the foot-point at frame no. 125. However, the rate of change of acceleration decreases from the loop top to halfway along the loop leg at 76 m s^{-2}, to 60 m s^{-2} from the loop leg to the foot-point. As the coronal rain clumps fall along the loop arcade, they encounter an increasingly more dense atmosphere at the loop foot-points in the TR and on into the chromosphere. The reduced acceleration in the rain has also been observed in quiescent coronal rain (Antolin & Rouppe van der Voort 2012), and this was confirmed numerically to be due to the increase of gas pressure in the lower atmosphere with the greater local densities (Fang et al. 2013).

In Figure 9, we can detect the ribbon formation in the early time frames in all AIA EUV channels (using the same cross-cut curve). This is most notable in the hottest AIA channel 9.4 nm, where we detect the continuation of the coronal flaring plasma along the length of the curve toward the loop top, between frame no. 65 and frame no. 86. When we look at the equivalent time–distance diagrams from the EUV channels for the 19.3, 17.1, and 30.4 nm images, we can identify the same bright coronal rain source in the EUV within the yellow box at the loop top. From this source, again we detect bright flows extending away from (marked with red arrows) and returning to the foot-point, in conjunction with the Hα strands in the line core time–distance diagram. In particular, we detect more clearly distinct bright tracks in the TR channel of 30.4 nm

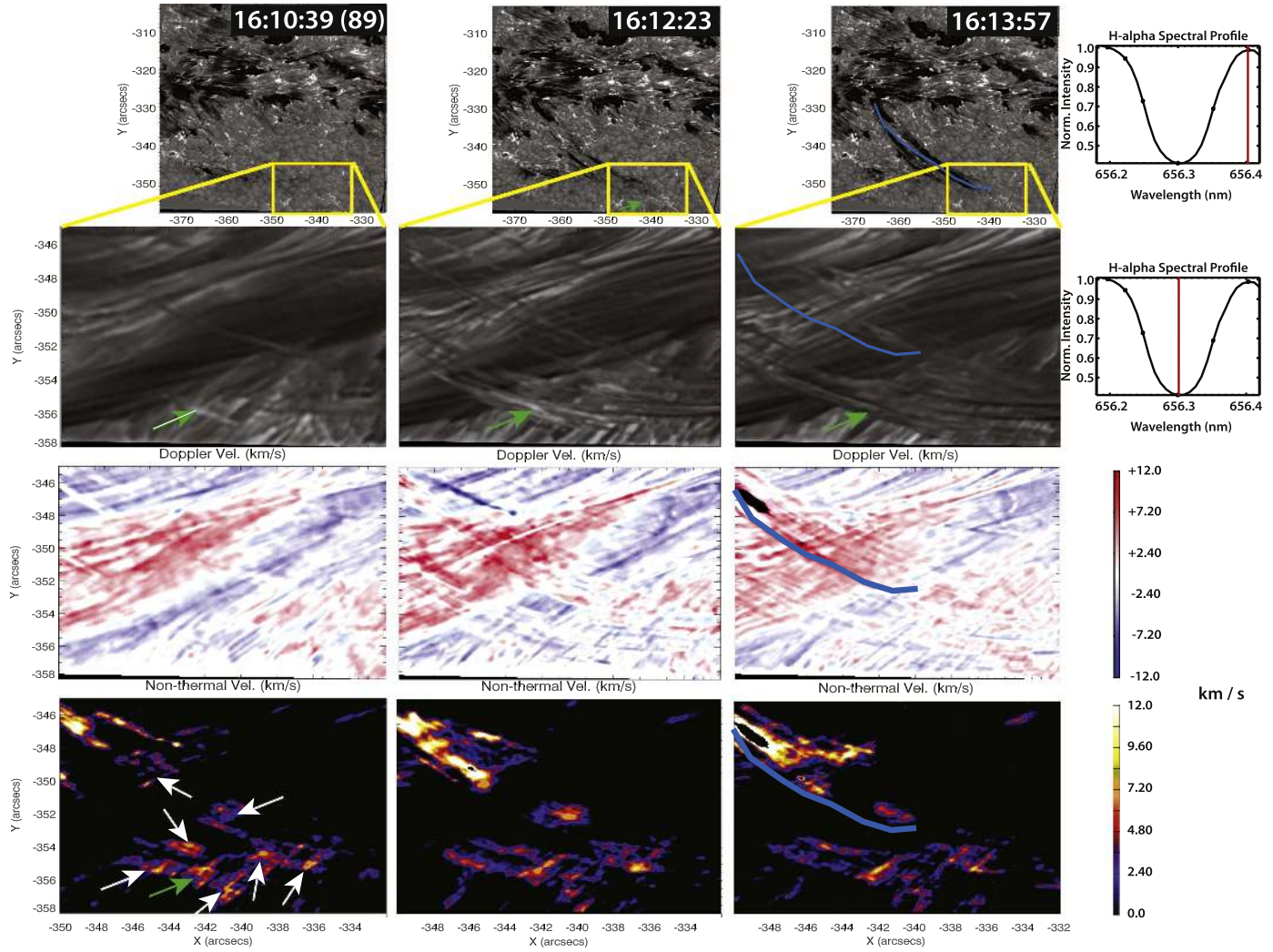

Figure 4. First row: within the CRISP full FOV (between 16:10:39 UT and 16:13:57 UT), we observe the formation of the dark coronal rain flow, along the trajectory of the postflare loop arcade (as marked by the blue curve) within the gray scale image of the Hα far red wing (+0.1032 nm). Second row: we present the zoomed FOV, as outlined by the yellow box, for the Hα line core. The blue curve is again overlaid in the third panel for perspective, and we reveal the evolution of the first detected loop-top coronal rain source with the green arrows. The spectral positions denoting the gray scale images of the first and second rows are marked as red lines within the Hα spectral scan in the fourth panels of these rows. Third row: dopplergrams are presented, as derived from the Hα spectral profile for each spatial pixel, from within the yellow box FOV. The spectral resolution is 6 pm, providing an error in the velocities of ± 0.3 km s^{-1}. Fourth row: the background-subtracted (i.e., using before and after images of the coronal rain formation region to remove the presence of underlying fibrils) line-width broadening maps are used to derive the nonthermal speed from measuring the FWHM change between the Hα spectral profiles at the location of the rain formation and the quiet Sun reference profile. The first detected rain source is marked with a green arrow.

farther along the loop leg. The hottest signatures at the coronal rain source appear first at frame no. 86 (as marked with the red dashed line), that is, two frames prior to the first detection in the cooler chromospheric lines. The colocation of the hot and cool components of the sources needs to be carefully considered due to line-of-sight effects. A better estimation of the temperature evolution from a DEM analysis, incorporating the intensity contributions from all AIA flaring channels, will be carried out in the next section.

The white, horizontal dashed line in Figure 9 is extracted to produce the light curves of Figure 10. In Figure 10, we present the normalized-intensity light curves of the EUV and chromospheric signatures for comparison, during the rain formation. The separation of the peaks of the respective channels in the EUV highlights the previous point regarding the presence of a rapid cooling process of only a few minutes. Between time frames no. 86 and 93 (bounded by the red box), we observe the peak in the EUV, together with the first appearance and increasing brightening of the coronal rain source in Hα and Ca II before absorption and decreased intensity after frame no. 93. The separation of the bright EUV peaks during the formation of the coronal rain at the loop top is on average 27 s.

In Figure 11, we present the spatial correspondence between the discretized location of the initial Hα rain bright loop-top source (contoured using 30.4 nm intensity contours) at 16:10:19 UT (frame no. 88) and its hotter multithermal components in 30.4 and 171. nm, which appear prior to the chromospheric component at 16:10:04 UT in 30.4 nm and 16:09:44 UT in 17.1 nm. From imaging in narrow-band spectral channels, there is clearly evidence for cooling of the rain source from the EUV to the visible channels, which appears within the contoured region, and the formation region is highlighted with the white arrows. The subsequent increase in the spatial size of the source and its intensity in all channels suggest we can expect a corresponding increase in the EM at this source, as gradually more plasma condenses to the

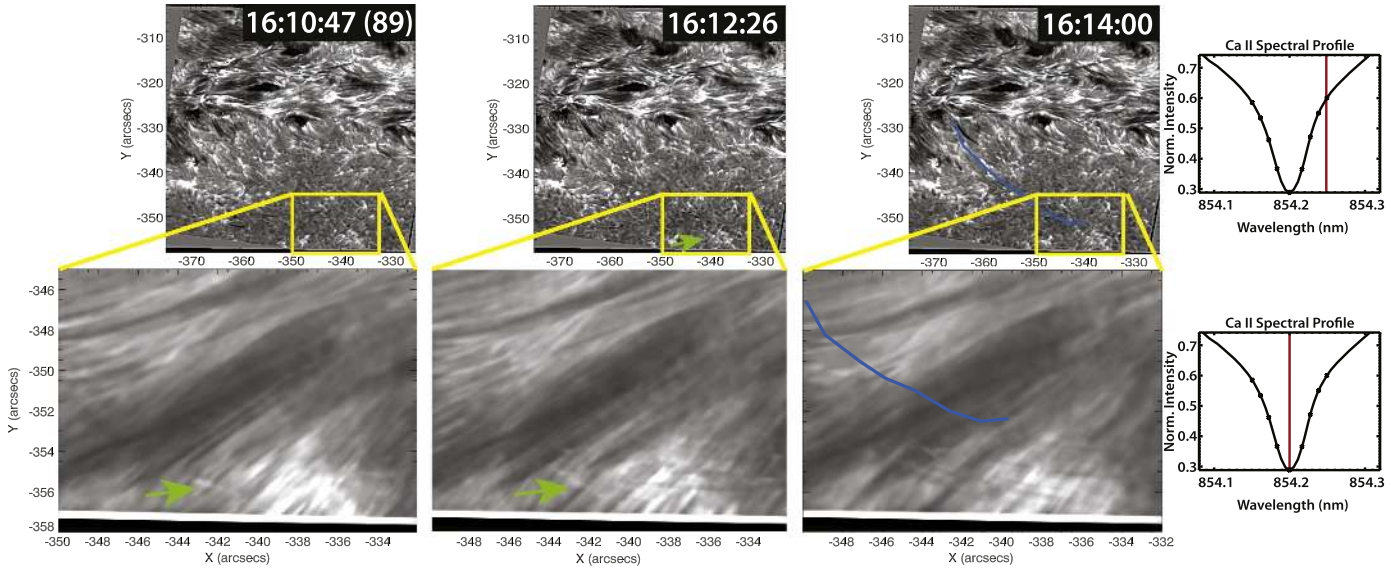

Figure 5. Top row: the gray scale images, as observed in the Ca II 854.2 nm red-wing (+0.0495 nm) channel, are presented for comparison with Figure 4. We mark the blue cross-cut curve for reference with the Hα images of Figure 4 and the yellow box of the coronal rain formation region. Bottom row: as compared with Figure 4, we present the Ca II 854.2 nm line core images, and the green arrows indicate the coronal rain source signature in emission. The Ca II 854.2 nm spectral profile is presented in the fourth panel in each row, with the corresponding spectral positions for the images marked with a red line.

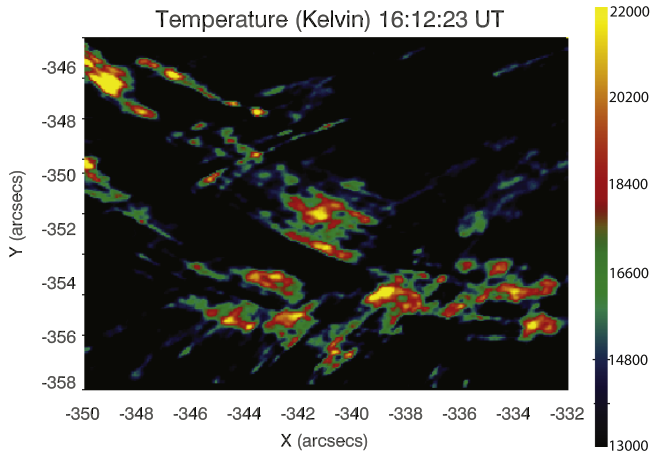

Figure 6. The temperature map of the yellow box region (i.e., defining the Hα coronal rain formation region outlined in previous figures) is presented for 16:12:23 UT (124 s after the first appearance of a source of coronal rain). Multiple (at least eight) relatively hot sources (≥22,000 K) of coronal rain are near the loop top. These temperatures represent an upper limit of the true temperature, obtained assuming negligible nonthermal velocity. A background subtraction has been applied to remove the presence of underlying fibrils using before and after images of the rain formation (note that the background fibrils are longer-lived features and hence easily subtracted).

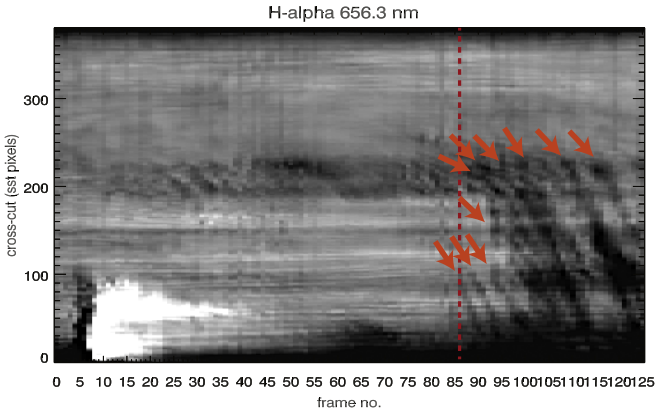

Figure 7. Time–distance diagram from the Hα far red wing (+0.1032 nm) FOV, using data extracted along the blue curve and averaged over multiple locations as the blue curve was scanned between the boundaries of the EUV postflare loop, as bounded by the green contours in Figure 3. The diagram therefore reveals the changes in the chromospheric rain flows on average across the width of the EUV loop. The *y* axis (distance along the curve from foot-point to loop top) increases from zero (the apparent foot-point in the flare ribbon) to 370 *SST*-pixels, that is, the apparent loop top, where the coronal rain formation is located within the yellow box region. The *x* axis (time) increases from a frame corresponding to 15:41:20 UT (during the preflare phase). The red arrows mark the formation of individual rain strands along the loop leg after loop-top rain formation. The vertical red dashed line is the time frame corresponding to the first signature of the loop-top source (as presented in Figure 11).

coronal/TR temperatures. The rain source appears as a spatially discretized source in the coronal channel 17.1 nm at 16:09:44 UT, and this relatively faint (contoured) source becomes more intense and more elongated along the trajectory of the loop. Then multiple sources become detectable by 16:10:39 UT. A similar growth rate of the source (spatially) occurs in the 30.4 nm channel and later in the Hα channel. This one-to-one correspondence between the spectral channels, its cospatiality and the corresponding spatial evolution, leads us to suggest that this source in the visible channels is indeed colocated (in three-dimensional space) with the EUV channel, and, therefore, we demonstrate the multithermal nature of coronal rain at the source of its formation. In other words, the given rain strands must be structured with both hot and faint and cool and dense plasma.

In Figure 12, we present the continued evolution of this initial rain source from the loop top and then along the loop leg in Hα and 30.4 nm, after its appearance as presented in Figure 11. Figure 12 reveals the continued spatial correspondence of the flow of the rain for the Hα and 30.4 nm signatures. As the Hα signature of the rain transitions from emission to absorption away from the loop top, we similarly detect a reduction of the intensity in the 30.4 nm component within the time range.

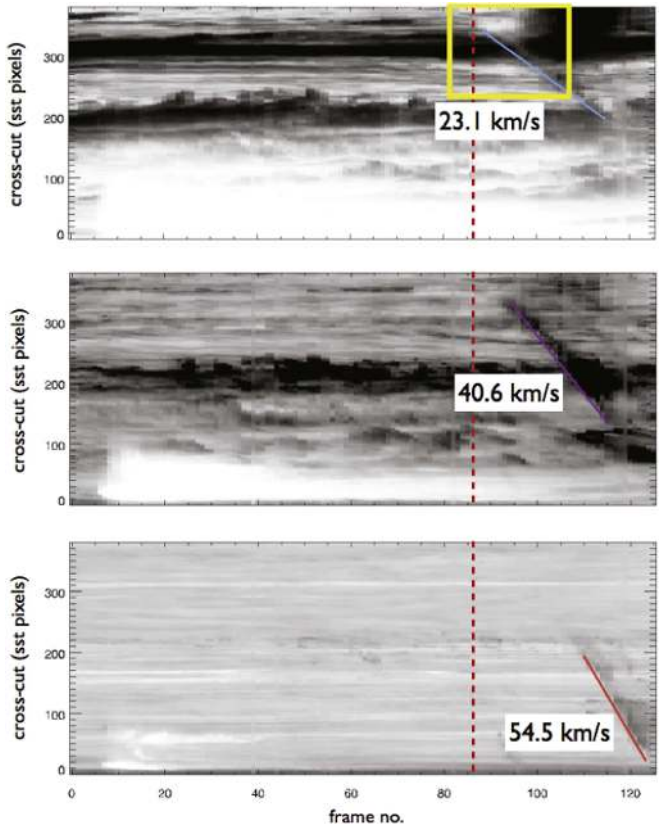

Figure 8. Time–distance diagrams from the Hα line core (top), near red-wing (+0.0774 nm: middle) and far red-wing (+0.1032 nm: bottom) spectral images, using the data along the blue curve from Figure 3 (right panel). The vertical, red dashed line is the time frame corresponding to the first signature of the loop-top source (as presented in Figure 11). The loop-top coronal rain bright emitting source (top side within the yellow box) and the subsequent formation of the rain strands in absorption (i.e., blue to purple to red solid lines) become more redshifted in time, and the acceleration decreases in time along the trajectory of the EUV loop leg.

At a later time, we detect further evidence for the colocation of the spatially evolving rain strand signatures within different spectral channels, highlighting again the multithermal nature of coronal rain, as shown in Figure 13. Here we present the temporal evolution (top row to bottom row) along the loop leg, whereby the loop top is at the bottom-right corner and the foot-point is at the top-left corner of each panel. The trajectory of the loop leg is very bright and well defined within the 19.3 nm image at 16:09:05 UT (panel A), where the plasma is expected to be at least 1–2 MK. After 59 s, we have a strong component of the same appear in emission in the 17.1 nm image (panel B). After an additional 55 s, we detect a clear signature of a localized coronal rain source in the 30.4 nm image (panel C) and a subsequent detection within the cotemporal Hα red-wing image in the same contoured region from 30.4 nm. In the next time frame, we observe a clear extension of this rain source along the same 19.3 nm loop leg in both 30.4 nm (faint and elongated) and Hα (dark and extended) in the direction of the foot-point from 16:12:23 UT to 16:13:22 UT. We find strong evidence to suggest the presence of a multithermal flow in flare-driven coronal rain strands. Given the time cadence between successive rows in Figure 13, we expect that the full half-length of the loop under investigation completely transitions from being hot and dense to having both hot and cold components with local regions of higher density in less than 4 minutes. Of course, at the beginning of the formation of the rain strand (in the rain source), this must be taking place at a faster rate. We expect that the catastrophic cooling process occurs during this time window.

4. REGULARIZED *SDO*/AIA DEM INVERSIONS

In order to understand the evolution of multithermal components of coronal rain, we must investigate in more detail the temperature contributions to the AIA passbands. We can then measure the temperature evolution from the X-ray band (as measured with *GOES* in soft X-ray channels) through to the EUV channels to finally become detectable as coronal rain strands at chromospheric temperatures.

To interpret the temperature contributions within the AIA FOV for each EUV channel in flaring conditions, we adopt a novel approach to calculating the DEM, through applying a generalized regularized inversion procedure, as developed by Hannah & Kontar (2012). The DEM ($\xi(T)$) quantifies the amount of plasma emitting within a certain temperature range and relates to the electron density of the plasma (n_e) as $\xi(T) = n_e^2\, dV/dT$, where V is a volume element that will be determined from the pixel area of the EM maps and an atmospheric column depth estimation, and T is the plasma temperature. We can investigate the DEM per pixel within a given temperature bin across the FOV of the postflare arcade in order to (1) investigate the temperature variations during the formation of the coronal rain source and (2) extract information about catastrophic cooling leading to rain formation from analysis of the local density variations and subsequent effects on the radiative cooling timescale, addressed further in the discussion section.

Hannah & Kontar (2012) constructed a model-independent regularization algorithm that makes use of general constraints on the overall form of the DEM versus temperature distribution, in this case in flaring conditions. Assuming optically thin emission in thermal equilibrium (we consider the postflare phase beyond flare heating leading to nonthermal equilibrium), the DEM is related to the observed data set g_i (observed intensity per AIA spectral channel (i) per pixel) as

$$g_i = \int_T K_i \xi(T) dT + \delta g_i, \tag{2}$$

where δg_i is the associated error on g_i, and K_i is the temperature response function (for AIA in this case). This ill-posed inversion problem needs to be stabilized. To do so, the algorithm introduces extra information by way of a smoothness condition on the source function. By making a prior assumption of the smoothness factor and inverting the data with regularization (Tihonov 1963), the algorithm can reliably infer physically meaningful features, which are otherwise unrecoverable from other model-dependent approaches such as forward fitting (refer to Kontar et al. 2004 for more information). This method has the added advantage of providing errors on the temperature bins through estimation of confidence levels when directly calculating the derivatives and then smoothing the solution to return the DEM. The regularized inversion directly solves the minimization problem, relating the data set to the expected CHIANTI (Dere

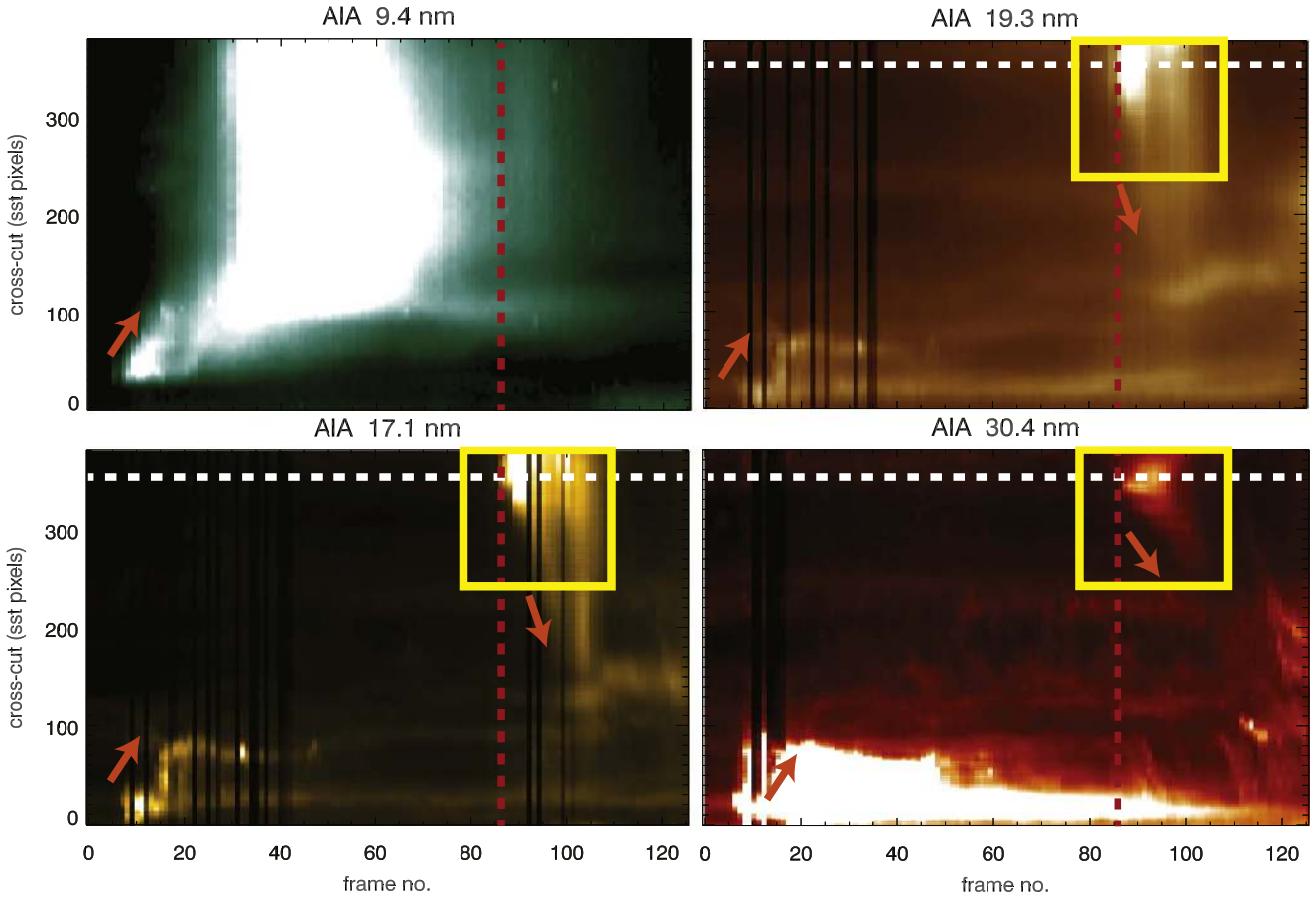

Figure 9. Time–distance diagrams are extracted along the same blue curve (as a direct comparison with Figure 8) but for cospatial and cotemporal AIA flaring spectral channel 9.4 nm (top left), coronal channels 19.3 nm (top right) and 17.1 nm (bottom left), and the transition region (TR) channel 30.4 nm (bottom right). We detect the bright coronal rain formation source (bounded by the yellow box) at the loop top and the subsequent rain strands or flows down the loop using downward-pointing orange arrows. The upward-pointing orange arrows represent the outward propagation of emission in the flare ribbon source in AIA along the loop early on. The red vertical dashed line represents frame no. 86, which is the time we first detect the hottest coronal rain source. The white horizontal dashed line, which passes through the coronal rain source, is used to produce the light curve of Figure 10, for all channels under discussion.

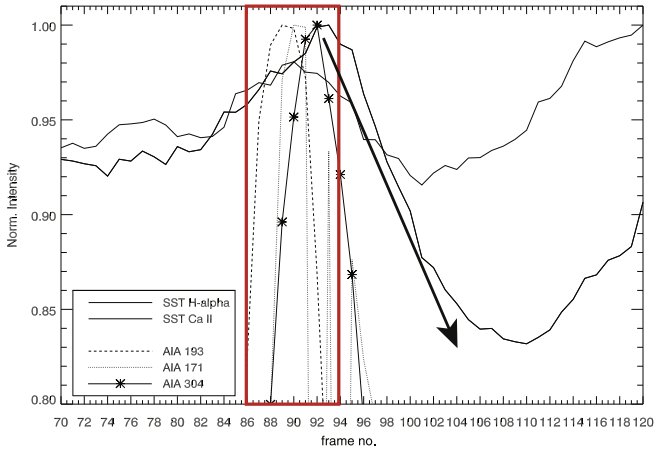

Figure 10. Light curves are extracted from the time–distance diagrams of Figure 9 (see horizontal, white dashed line) for AIA channels 19.3, 17.1, and 30.4 nm and overlaid with CRISP Hα 656.28 nm and Ca II 854.2 nm channels from Figure 8. The legend distinguishes the lines corresponding to different channels. The black arrow marks the onset of the chromospheric component of coronal rain and the resulting decrease in the intensity at the loop-top source, in both Hα and Ca II.

et al. 1997; Landi et al. 1999) DEM model. Here we assume a CHIANTI DEM model for flaring conditions. Using these constraints, the inversion problem outlined in Equation (2) can be restated as

$$\|\tilde{\boldsymbol{K}}\xi(T) - \tilde{\boldsymbol{g}}\|^2 + \lambda\|\boldsymbol{L}(\xi(T) - \xi_0(T))\|^2 = \min, \qquad (3)$$

where the tilde represents normalization by the error, λ is the regularization parameter, $\boldsymbol{L}$ is the constraint matrix, and $\xi_0(T)$ is a possible guess solution. We refer to Hannah & Kontar (2012) for a full description of the method, which has been applied in many cases involving active-region coronal loop systems as observed with *SDO* (Aschwanden & Boerner 2011; Foullon et al. 2011; Reeves & Golub 2011; Warren et al. 2011; Hannah & Kontar 2012). The regularization method has been very successfully applied to flare studies using *RHESSI* data for electron flux and density distribution reconstruction, as outlined by Kontar et al. (2004) and Kontar & MacKinnon (2005).

The regularized inversion approach adopted here for calculating DEMs for the observed AIA data set will enable an accurate interpretation of the plasma temperature and density variations at the coronal rain source, since information from all spectral channels is incorporated. It is highly likely, from our analysis of the EUV data, that the coronal rain source is multithermal, so a multitemperature analysis of the source will help to interpret how the thermal components within the rain source evolve in time and spatially across the FOV. In

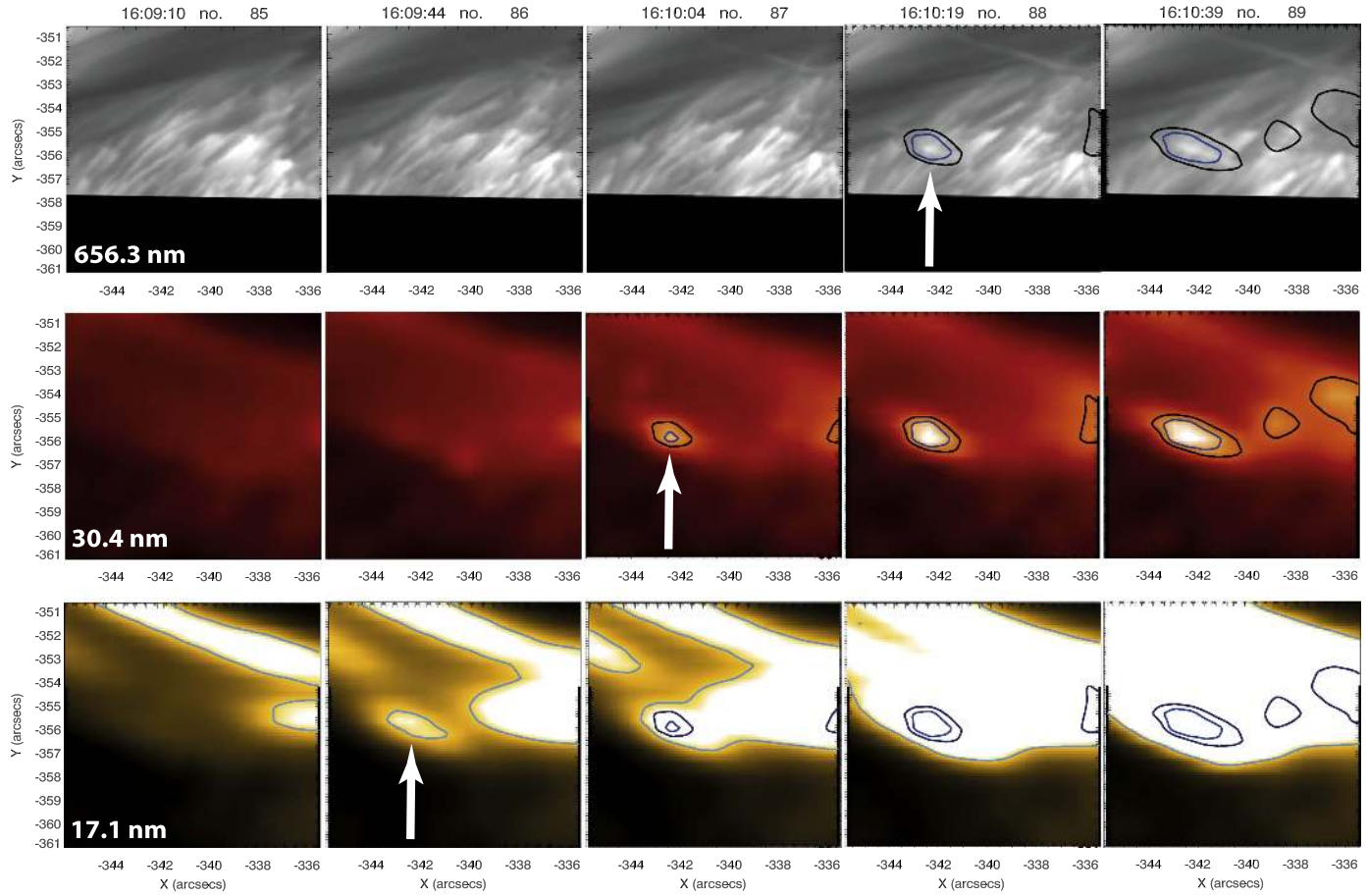

Figure 11. We reveal the multithermal, cospatial signatures of the coronal rain loop-top source at the time of its formation. The white arrows mark the location of the rain source in each spectral channel when it first appears. The arrows demonstrate the order of appearance of the source, becoming detectable in the lower temperature channels. The contours of the 30.4 nm (middle row) channel are overlaid onto the Hα core images (top row), and, similarly, they are superimposed together with 17.1 nm contours on the 17.1 nm images (bottom row). The temporal evolution of the multithermal properties of this loop-top rain source, corresponding to the peak temperature of the respective passbands, appears as star symbols within the summarizing light curve of Figure 20.

Figure 14, we present the data input from each spectral channel at the time of the rain formation (at frame no. 86). In all of the AIA channels presented, we can see clearly the formation of the postflare arcade in all spectral channels. Most notably, in the 17.1 nm image, we can detect the spatially correlated bright coronal rain source that was revealed within the AIA time–distance diagrams of Figure 9 (i.e., the yellow box region). In Figures 15–17, the top-row panels represent the emitting plasma contribution at below 1 MK, and the bottom row represents the plasma DEM for temperature contributions greater than 1 MK, across the FOV.

From Figure 15, we sample the EM before the formation of the coronal rain in frame no. 82 (corresponding to 16:08:15 UT). At this time, the postflare arcade is filled with plasma in emission at greater than or equal to $1 \times 10^{23}\,\mathrm{cm}^{-5}\,\mathrm{K}^{-1}$ (bright red structures) in the Log $T = 6.6$–6.8 temperature range. As expected, there is no significant emission within the FOV below 1 MK at this stage in the postflare decay phase. The EUV postflare arcade has formed after the decay of the X-ray signal from *GOES* at this time (see Figure 2), whereby the X-ray flux has returned to background levels.

In Figure 16, we detect a notable decrease in the DEM in the loop (i.e., within the yellow-boxed rain source region) at 16:09:44 UT. The postflare arcade now contains more patchy red regions and reduced EM per pixel in the $\mathrm{Log}_{10}\,T = 6.6$–6.8 temperature range, corresponding to a DEM of 6–7 $\times\ 10^{22}\,\mathrm{cm}^{-5}\,\mathrm{K}^{-1}$. We expect that catastrophic cooling is established or ongoing in this time prior to its first appearance in the chromospheric channels 35 s later (16:10:19 UT). In the top-right panel of Figure 16, we detect the faint outline in the DEM map of the submillion kelvin postflare loop and associated EUV coronal rain source, which extends toward the foot-point of the flare ribbon at [30, 45] in solar x/y. This loop signature in TR plasma follows the trajectory of the Hα rain flows as defined by the blue curve cross-cuts in previous figures.

In Figure 17, we present the cooling of the loop 159 s later (16:12:23 UT), and the EM has increased in the TR plasma, as the Hα rain flow extends from the loop top to the loop leg. At this stage, the DEM at the loop top is now at background levels with respect to the plasma at temperatures of $\mathrm{Log}_{10}\,T = 6.6$ (4 MK), and at the same time the DEM at $\mathrm{Log}_{10}\,T = 5.8$ has increased significantly to $6 \times 10^{22}\,\mathrm{cm}^{-5}\,\mathrm{K}^{-1}$, and the postflare arcade is clearly visible at temperatures below 1 MK. Next, we will investigate the DEM versus temperature profiles associated with the source of the coronal rain formation within the yellow box, as marked by the black cross in Figures 15–17, to understand the evolution of the loop cooling process in more detail.

In Figure 18, the DEM versus temperature profiles within the rain source evolve in time from top left to bottom right. In

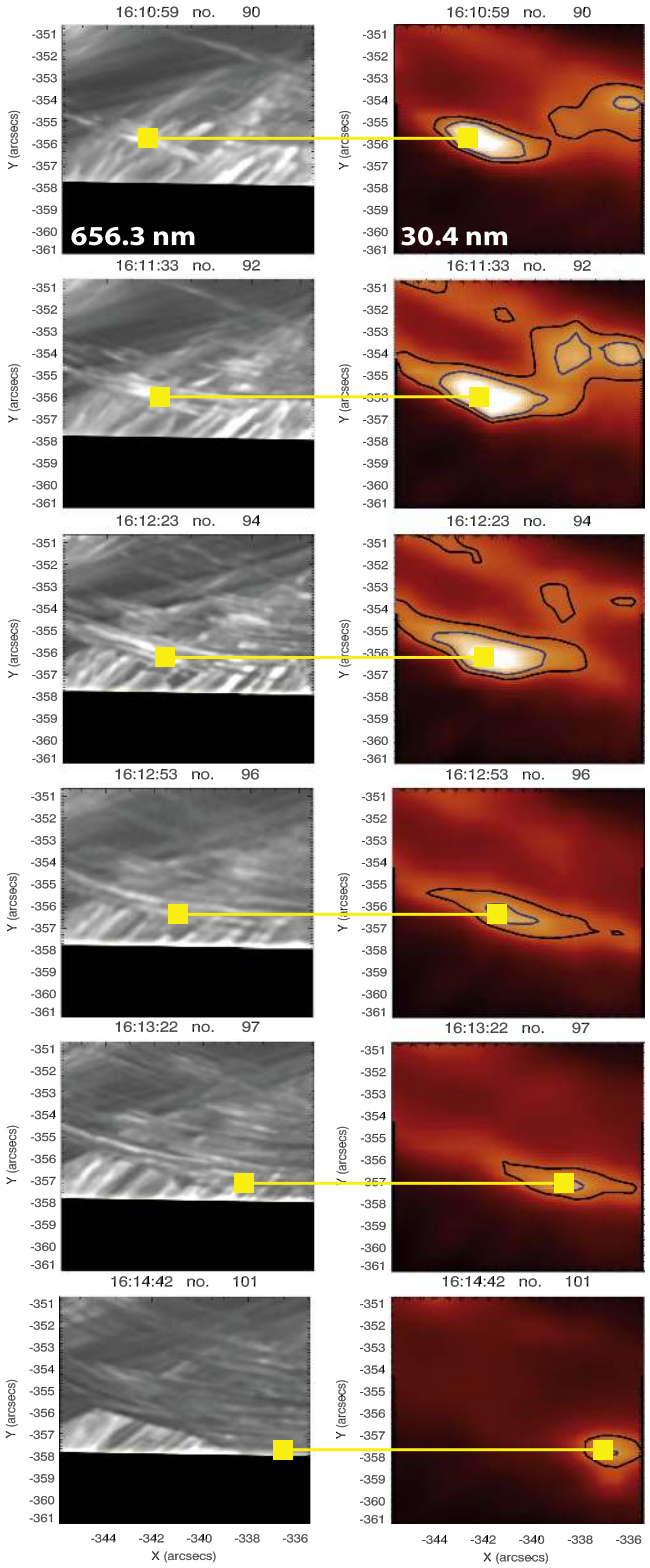

Figure 12. We present the cospatial, multithermal flow of a bright Hα loop-top coronal rain source after its formation (as presented in Figure 11). The images evolve in time from top (16:10:59 UT) to bottom (16:14:42 UT), and we present the Hα core images in gray scale on the left-hand side and 30.4 nm images on the right-hand side. The corresponding flows in both channels, along the loop from left to right (spatially in the FOV), are represented using the horizontal, yellow solid lines in each row.

general, we reveal the migration of all DEM peaks from right to left, leading to greater EM for progressively lower temperature plasma in time. For instance, between 15:59:10 UT and 16:06:56 UT, the EM in the highest-temperature bin (having a peak at $\mathrm{Log}_{10}\,T = 6.8$ and marked with the vertical, blue dashed line) reduces extensively in DEM. Simultaneously, we detect a progressive increase in the EM in the temperature range of $\mathrm{Log}_{10}\,T = 6.5$ (as marked with the vertical orange dashed line). Hence, within 466 s a large component of the plasma temperature at the source has dropped by ~3.1 MK, which corresponds to at least 6500 K s^{-1}. Later, between 16:08:15 UT and 16:09:44 UT, this plasma temperature peak, as marked with the orange dashed line, appears to migrate from $\mathrm{Log}_{10}\,T = 6.5$ to $\mathrm{Log}_{10}\,T = = 6.4$, which corresponds to an even faster rate of cooling of 7300 K s^{-1}. The yellow arrows (bottom row of Figure 18) highlight the relatively large changes in the DEM at the coronal rain source when plasma emitting at greater than 1.5 MK ($\mathrm{Log}\,T = 6.2$) at frame no. 86 reduces in EM, while plasma at ~0.5 MK substantially increases by frame no. 90 (16:10:59 UT). Notice the peak at $\mathrm{Log}_{10}\,T = 5.7$ (corresponding to TR plasma emission) has approximately the same emitting contribution as the peak at $\mathrm{Log}_{10}\,T = 6.2$, indicating that most of the plasma is cooling to submillion kelvin temperatures. This process occurs during the first appearance of the chromospheric component of the rain in its formation, supporting the argument that the source is indeed multithermal, as well as being very thermally active. By tracking the migration of the DEM peaks in the DEM versus temperature profiles at the rain-formation site, we can interpret the temporal evolution of temperature (see Figure 19 right) and EM (see Figure 19 left) at the source.

In Figure 19 (left panel), we discover the sudden increase in EM from frame no. 73 (16:05:26 UT) to frame no. 82 (16:08:15 UT). This increase corresponds to the response of the coronal plasma increasing in emissivity in the temperature range of 1.5–7 MK. Figure 19 (right) confirms that during this time interval we detect a continuous cooling of the coronal plasma. The large orange arrow marks the time of the peak in this period of increased EM of the coronal plasma, which occurs at frame no. 82 (16:08:15 UT). Next, within four frames (89 s) until 16:09:44 UT, the cooling into the 17.1 nm passband becomes detectable at the loop-top source from imaging, that is, the first signature of the local rain formation present in Figures 11, 13 (panel B), 14, and 17. In Figure 19, the commencement of the TR plasma emission, at below 1 MK, is marked with a black dotted line, which we define as the start of catastrophic cooling, referred to herein as phase V. Between frames 82 and 86, the EM has started to decrease in the coronal loop-top plasma, and cooling starts to become dominant in TR plasma. Until 16:10:19 UT (an additional 35 s from frame no. 86), we have a short period of accelerated cooling to chromospheric temperatures at this source, leading to the appearance of the source in Hα in emission followed by absorption, and this interval coincides with a further increased contribution from plasma in emission at ~0.5–1 MK in the loop leg. In summary, the time interval through which catastrophic cooling occurs, when the temperature at the loop-top source drops by ~1.5 MK, is greater than 35 s and less than 124 s, at the start of the decline the corona plasma EM peak (see orange arrow in Figure 19 left) and the first appearance of the

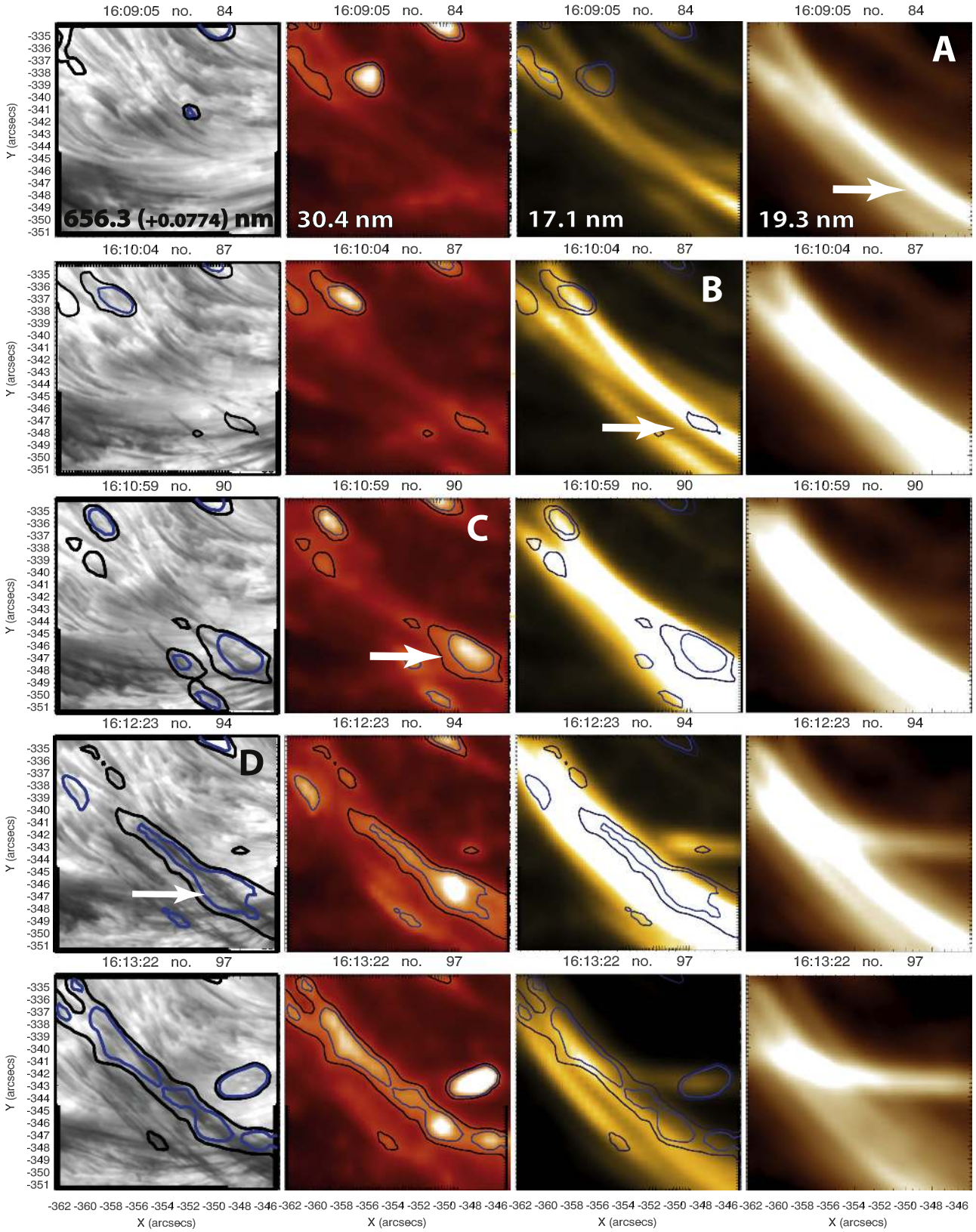

Figure 13. The cospatial, multithermal flow of another coronal rain strand from a bright Hα loop-top coronal rain source, along an opposing loop leg (i.e., compared with the loop-leg strand from Figure 12). Temporal evolution is from top to bottom (from 16:09:05 UT to 16:13:22 UT), and the cospatial spectral images evolve from the visible (Hα red-wing image at +0.0774 nm) into the hotter EUV channels (30.4, 17.1, and 19.3 nm) from the left to the right panels. The white arrows depict the first clear detection of the rain source within the loop leg, in each respective channel. The trajectory of the loop leg is very bright and well defined within the 19.3 nm image at 16:09:05 UT. This evolution through the spectral channels is also labeled A–D in the respective panels. The contours of 30.4 nm are overlaid in all panels (except in the 19.3 nm panels) for context. Time stamps concerning the formation of this coronal rain source and strand, in each spectral channel, appear as symbols within the summarizing light curve of Figure 20.

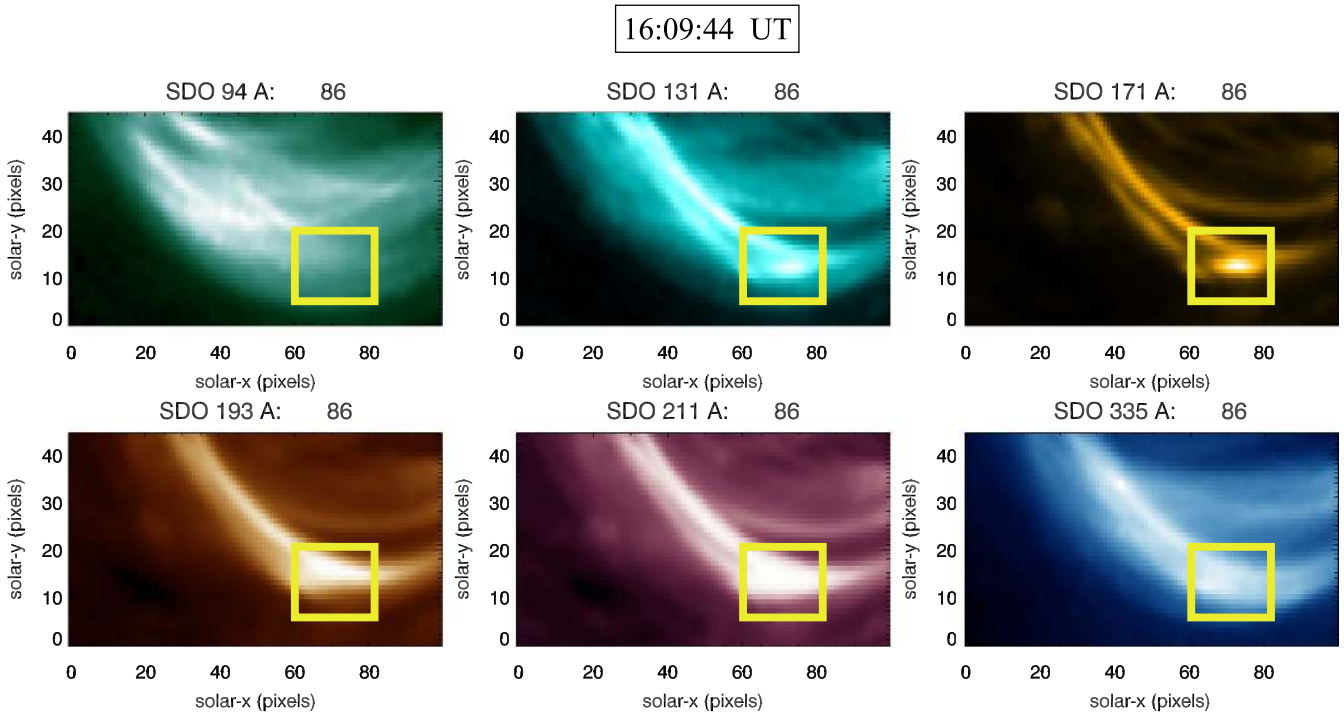

Figure 14. All AIA coronal spectral images of 9.4, 19.3, and 17.1 nm (top row) and 19.3 nm, 21.1 nm, and 33.5 nm (bottom row) are presented for time frame no. 86 (16:09:44 UT). This time corresponds to the earliest detection of the coronal rain source within the EUV channels, as determined from the time–distance diagrams. This bright coronal rain source is colocated within the yellow box at the postflare loop top, as was previously presented for the bright chromospheric source in Figure 4 for Hα and Figure 5 for Ca II, which first appears at 16:10:47 UT.

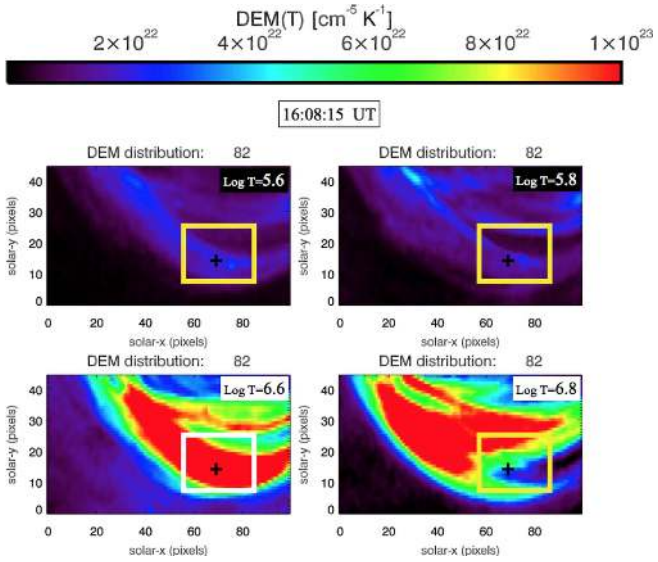

Figure 15. The output from the DEM inversion code for calculating the EM in each pixel across the FOV, before the formation of the EUV coronal rain loop-top source at 16:08:15 UT (frame no. 82). The EM is plotted as a function of increasing temperature in each panel from top left to bottom right. The top two panels detail the amount of plasma that is in emission with a temperature *below* 1 MK. The bottom two panels detail the amount of plasma that is in emission with a temperature *above* 1 MK up to $\mathrm{Log}_{10}\,T = 6.8$ (6.3 MK). The yellow box is overlaid for context as the location of the chromospheric component of the coronal rain source at the loop top. The black cross highlights the location of the coronal rain source within the yellow box from Hα and Ca II, which will be investigated in detail in Figure 18.

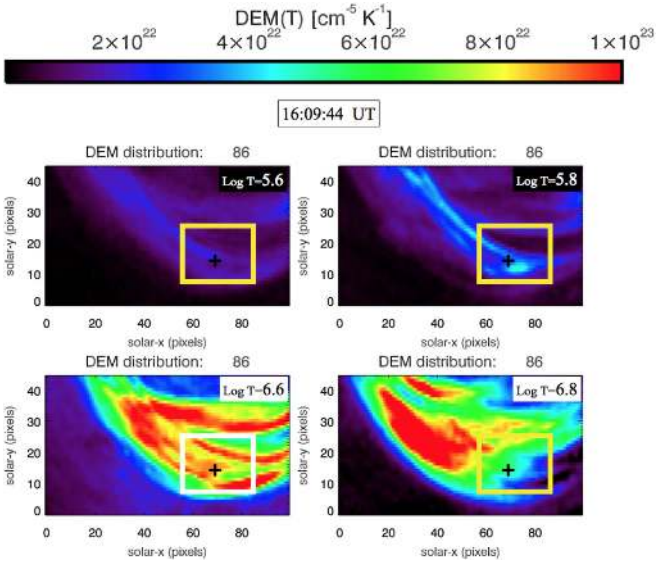

Figure 16. Output from the DEM inversion code for calculating the EM in each pixel across the FOV, at the time of the formation of the EUV coronal rain loop-top source, that is, at 16:09:44 UT (frame no. 86). The same format applies as for Figure 15.

chromospheric component of the rain (see red dashed line in Figure 19 right).

In order to place the catastrophic cooling process leading to coronal rain formation in the context of postflare loop cooling, we have appended the *GOES*, AIA, and CRISP temperature profiles into a summarizing cooling curve in Figure 20. This cooling curve uniquely connects the hottest components at the flare temperature peak with the formation of the chromospheric component of the coronal rain strands at the loop top and shortly after in the loop legs. From Figure 20, we reveal five phases in the cooling process, as bounded by the vertical dashed lines, and these regions are banded in different colors. The physical interpretation of this summarizing cooling curve

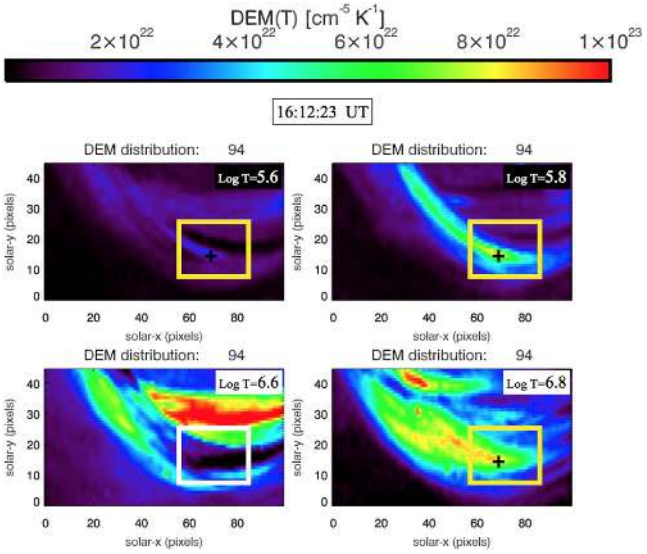

Figure 17. Output from the DEM inversion code for calculating the EM in each pixel across the FOV, after the formation of the EUV coronal rain loop-top source, that is, at 16:12:23 UT (frame no. 94). The same format applies as for Figure 15.

will form the basis of the discussion section, as well as provide new insights into the earliest onset of catastrophic cooling in the EUV prior to its appearance at chromospheric temperatures.

5. DISCUSSION

We reveal in detail a clear association between flare sources of chromospheric evaporation and the subsequent cooling of the heated plasma, which falls back to the same source as chromospheric coronal rain (see Figure 3). Dense clumps or strands of partially ionized chromospheric coronal rain flow in a multithermal stream along a trajectory prescribed by the postflare magnetic arcade. Subsequently, the chromosphere–corona mass cycle is investigated at the highest achievable resolution using *GOES*, *SDO*/AIA, and *SST*/CRISP instruments covering a broad spectral range spanning soft X-rays to the (E)UV, near-IR, and visible wavelengths.

During the flare impulsive phase, the plasma temperature peaked at ∼15.4 MK, via direct heating of the chromosphere, resulting in chromospheric evaporation (Antiochos & Sturrock 1976; Kopp & Pneuman 1976). Chromospheric evaporation can be driven by a number of heating mechanisms, aside from nonthermal particle beams (Battaglia et al. 2015), and it can be classified as either explosive or gentle (Fisher et al. 1985; Milligan et al. 2006a, 2006b). Thermal conduction from the corona can drive the expansion of hot, dense chromospheric material into postflare arcades, but eventually it is expected that the conductive heat flux will no longer compensate for the radiative losses in the corona, and the loops will rapidly begin to cool (Antiochos et al. 1999; Karpen et al. 2001). Radiative losses increase and dominate over conductive losses, and at a later stage a loop-top thermal instability leads to catastrophic cooling (i.e., accelerated cooling) to chromospheric temperatures, and we observe a substantial loop drainage or depletion, as observed here in Hα. During the thermal instability, the decrease in temperature in the loop is accompanied by a decrease in pressure, which then accretes plasma from the surrounding atmosphere, leading to the localized formation of dense rain condensations (Goldsmith 1971; Hildner 1974; Antiochos & Klimchuk 1991; Müller et al. 2004; Fang et al. 2013). Clumpy condensations eventually become dense enough to fall under gravity back to the surface (overwhelming the opposing magnetic pressure force of the loop arcade), resulting in a catastrophic depletion of plasma in the loop. The postflare loop cooling through the soft X-ray to EUV channels, leading to the formation of localized dense clumps of multithermal coronal rain in Hα, first in emission then in absorption, has not been observed until now.

To do so, we employ the hydrodynamic zero-dimensional (0D) model by Cargill et al. (1995), which describes the cooling of postflare loop plasma during the flare decay phase and can be used to interpret the timescales associated with the cooling curve of Figure 20. After a detailed statistical analysis, it was found that the Cargill model provides a very well defined lower limit on flare cooling times and that radiation is the dominant loss mechanism throughout the cooling for 80% of flares (Ryan et al. 2013). For the remaining 20%, conduction dominates initially, before cooling becomes dominated by radiation. For simplification, we refer to 0D models such as the Cargill model, which assign field-aligned averages of the hydrodynamic properties of cooling loops, within the limits of an optically thin plasma at temperatures >1–2 MK. Field-aligned averages are justified by the fact that hydrodynamic properties (such as temperature, pressure, and density) do not vary much along the length of the coronal loop within the corona, except near the interface of the corona and TR, which is characterized by steep gradients. The 0D assumptions are considered to be acceptable in comparison with 1D models (Klimchuk et al. 2008). If the cooling curve from Figure 20 can be explained by known energy-loss mechanisms, we should expect that the onset of catastrophic cooling should occur within the expected timescale for radiative cooling. Next, we will calculate the energy loss rates due to conduction, radiation, and enthalpy-based radiative cooling, through considering the energy transport equation in cooling flare loops.

In order to simplify the problem of calculating the cooling rates in postflare loop arcades, the Cargill model assumes that the plasma is confined to the axis of the magnetic field (s), so there is unsubstantial cross-field diffusion of energy (i.e., strands of plasma are thermally isolated), which is an acceptable assumption under solar conditions, given the relatively short Debye length scales compared with the Larmour radius for particle collisions (note that fast thermal modes produced in numerical models of coronal rain can leak energy across fields). In this study we assume that field-aligned thermal conduction is dominant since that helps to explain why we observe very clearly defined plasma strands in loop arcades. Furthermore, we assume a single fluid approximation and do not consider the collisional energy loss rate between different particle species. The energy transport equation can then be written in the form as described in Ryan et al. (2013) as

$$\frac{1}{\gamma-1}\frac{\partial p}{\partial t} = -\frac{1}{\gamma-1}\frac{\partial}{\partial s}(p\,u_s) - p\,\frac{\partial u_s}{\partial s} + \frac{\partial}{\partial s}F_c - n_e^2\,\Lambda(T) + h, \quad (4)$$

where γ is the adiabatic constant, p is pressure, u_s is the plasma flow velocity along the axis of the magnetic field (s), F_c is the conductive heat flux, $n_e^2\,\Lambda\,(T)$ is the radiative loss rate

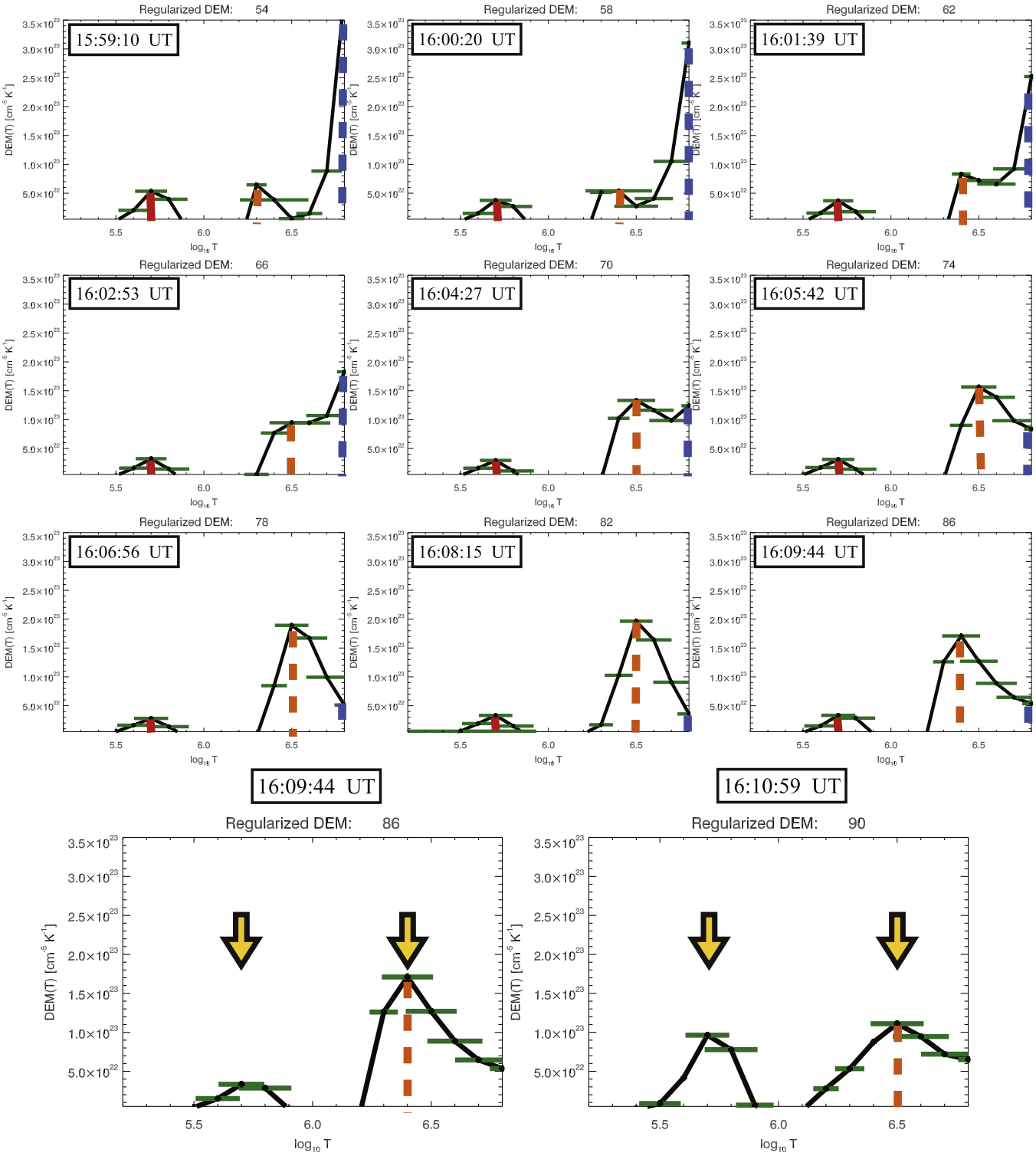

Figure 18. A group of five pixels from within the black cross of Figures 15–17 each contain a DEM vs. temperature profile that is averaged and reproduced in each panel here. The evolution of the temperature profile is demonstrated, from the top-left panel (frame no. 54, 15:59:10 UT) to the bottom-right panel (frame no. 90, 16:10:59 UT), and describes the conditions of the postflare loop top until the formation of the rain source. The vertical blue dashed line describes the evolution of the hottest detectable plasma emitting at 6.8 MK. The vertical, orange dashed line tracks the evolution of the second peak, which corresponds to coronal plasma temperatures. The vertical, red solid line describes the evolution of the plasma emitting at $10^{5.7}$ K. Each temperature bin has a measured temperature error and is overplotted in green. The yellow arrows highlight the relatively large changes in the EM between frame no. 86 and 90, indicating a transition from emission predominantly at coronal temperatures to TR temperatures. The error in DEM measurement at each temperature bin is $\pm 3 \times 10^{22}$ cm^{-5} K^{-1}.

(assuming optically thin conditions), and h is the heating rate per unit volume. The first and second terms on the right-hand side of Equation (4) represent energy losses due to flows within the cooling loop, which are associated with enthalpy-based radiative cooling as well as expansion and contraction of the loop. Here we assume that the loop does not appreciably

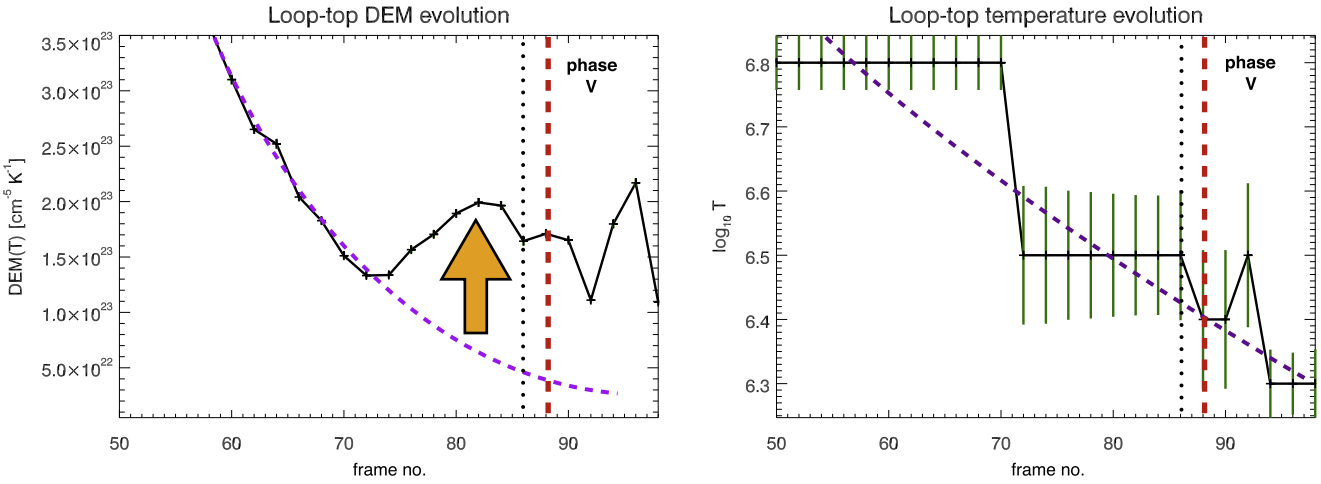

Figure 19. Through tracking the peaks in the DEM vs. temperature profiles of Figure 18, we reproduce the evolution of the temperatures (right panel) of the rain source in the EUV coronal plasma and corresponding coronal plasma DEM (left), with respect to frame number. The error in each temperature bin is overplotted in green. The vertical dotted line (frame no. 86 at 16:09:44 UT) defines the start of the catastrophic cooling phase (that is, phase V). The notable EUV EM increase demarcates the onset of cooling through to coronal plasma temperatures (from 7 to 1.5 MK), as shown with the upward-pointing orange arrow. The red, vertical dashed line corresponds to frame no. 88 (16:10:19 UT), marking the first appearance or formation of the chromospheric component of loop-top coronal rain. The purple dashed line is a second-order polynomial fit to these distributions.

expand or contract during the decay phase, so assumptions about the loop volume and length at the start of cooling are the same as those applied at the latest stages of cooling. It should be noted that the radiatively dominant phase is a result of energy loss not just by radiation but also by an enthalpy flux of mass flows falling down the loop legs (Bradshaw 2008). Enthalpy-based cooling becomes significant at the latest stages of flare loop cooling, and the enthalpy flux is considered to be important in balancing the TR emission and radiative losses (Bradshaw & Cargill 2010; Cargill & Bradshaw 2013). The third term on the right-hand side defines the conductive losses from the divergence of the heat flux, F_c, which is defined as $F_c = -\kappa \frac{\partial T}{\partial s}$, and $\frac{\partial T}{\partial s}$ is the temperature gradient. Here κ is the *Spitzer* thermal conductivity (i.e., $\kappa = \kappa_0 T^{\frac{5}{2}}$), such that $\kappa_0 \approx 10^{-6}$. The fourth term on the right-hand side represents the radiative loss rate, where $\Lambda(T)$ is the optically thin radiative loss function. A scaling law for $\Lambda(T)$ can be assumed (see review by Reale & Landi 2012), using the parameterization of Rosner et al. (1978), resulting in $n_e^2\ \Lambda(T) = n_e^{\zeta}\ \chi\ T^{\alpha}$.

The evolution and energy transport in the postflare arcade plasma is controlled by the balance between conductive and radiative losses, together with flows and decay phase heating processes (h), such as additional magnetic reconnection. Next, we will consider independently the cooling timescales due to each of these processes, using the derived properties from the observations.

5.1. Conductive Cooling

Reale (2007) defined four phases describing the evolution of confined plasma in flare loops. Here we characterize this flare along those guidelines and introduce a phase V for catastrophic cooling. Phases I and II describe the *heating* and *evaporation* of the plasma from the start of the flare heat pulse in the corona to the temperature peak T. The heat pulse is efficiently conducted to the cool chromospheric plasma, which is strongly heated and expands filling the loop with hot dense plasma. This results in a rapidly increasing EM offset from the temperature peak. Phase III corresponds to the *conductive cooling phase* and occurs between the end of heating and the EM peak by efficient thermal conduction (Cargill & Klimchuk 2004). Conductive cooling may account for faster cooling timescales in flaring conditions (Doschek et al. 1982) when the temperature gradients are largest. The conductive cooling phase starts at the temperature peak and continues to the peak of the EM (Cargill 1994), which is common in flare observations (Sylwester et al. 1993). In this flare, at the start of the cooling phase III, the temperature peaks measurably before the EM (see Figure 20). The conductive cooling timescale (τ_c) can be calculated by neglecting heating, radiative losses, and energy transport due to flow terms. The model can be further simplified by assuming that the plasma is isothermal and obeys the ideal gas law, whereby $p = \frac{3}{2} n_e\ k_{\rm B}\ T$, where $k_{\rm B}$ is the Boltzmann constant. Therefore, Equation (4) becomes

$$\frac{\partial}{\partial s}\left[\kappa_0\ T^{5/2} \frac{\partial T}{\partial s}\right] = \frac{k_{\rm B}}{\gamma - 1}\ n_e\ \frac{\partial T}{\partial t}. \quad (5)$$

After integration of Equation (5), one can derive an approximated relationship for the conductive cooling timescale (Cargill et al. 1995) as

$$\tau_c = 4\ \times\ 10^{-10} \frac{n_e L^2}{T^{5/2}}. \quad (6)$$

During phase III, starting at 15:44:30 UT when the temperature peaks at 15.4 MK (according to the *GOES* light curve), conductive losses dominate, and we can calculate the conductive loss timescale (using Equation (6)). From Figure 20 at the temperature peak, we measure the EM of $0.165\ \times\ 10^{49}$ cm^{-3}. In order to calculate the electron density from the *GOES* EM, we need to assume a volume of emitting plasma. Here we assume a volume of a cylinder describing the soft X-ray postflare loop with cylinder length equal to $2L$ and diameter of 10 arcsec, which is determined from the observations of the loop cross sections in AIA at a later stage in the cooling process (see inset panel of Figure 2). Taking the observed loop

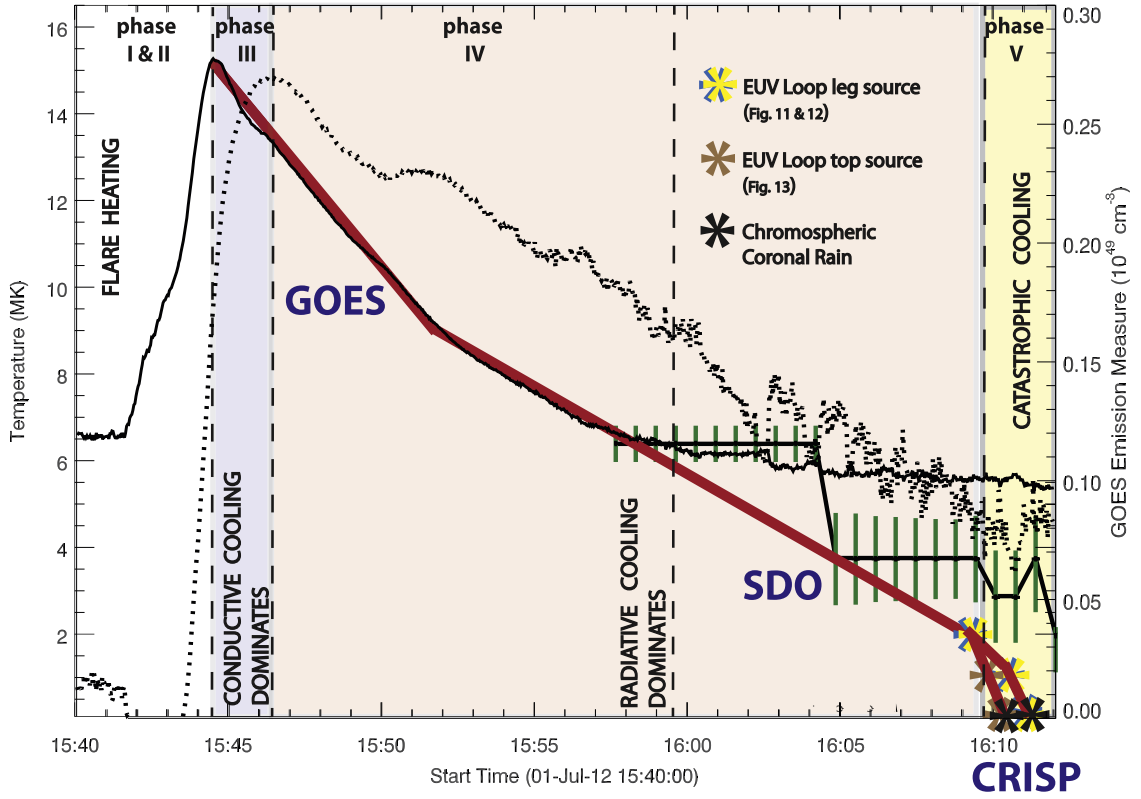

Figure 20. The cooling curve (red solid curve) extends from the temperature peak of the flare impulsive phase observed in *GOES* (solid black curve), through the EUV as observed with AIA (solid black lines with green error bars), until the start of the formation of coronal rain strands as observed with CRISP (star symbols). The temperature profile has its axis on the left-hand side. During the *SDO*/EUV stage, the cooling curve connects the start of the most prominent changes in the temperature evolution of the DEM vs. temperature profiles (see Figure 18). Five phases (I–V) describe the evolution of the dominant cooling processes, in accordance with Reale (2007), and these intervals are labeled and colored. The transition times for each respective cooling mechanism corresponding to these phases are calculated using the Cargill model and presented with vertical, dashed black lines. Phase I–II represents the heating or onset of the flare, phase III represents the dominant conductive cooling phase, phase IV represents the transition to radiative cooling, including the onset of the dominant radiative cooling phase (marked with vertical dashed lines), and finally phase V represents the start of catastrophic cooling. During catastrophic cooling, the red cooling curve splits into two branches, corresponding to loop-top coronal rain temperature evolution (brown symbols) and loop-leg coronal rain temperature evolution (yellow symbols). The black dashed curve is the *GOES* EM with axis on the right-hand side.

half-length (L) from the observations as $L = 3.2 \times 10^9$ cm, we hereby assume an emitting volume of 2.14×10^{27} cm^3, and with a filling factor of 1 we estimate an electron density at the start of phase III to be 2.77×10^{10} cm^{-3}, which is reasonable under flaring conditions. With these estimates we calculate the conductive cooling timescale of $\tau_c = 122$ s and hence a conductive cooling end time at ~15:46:32 UT, which indeed corresponds with the peak in the observed *GOES* EM. The assumption that the loop volume does not change appreciably between the start of the decay phase and the end is warranted, considering this clear correspondence between the model conductive cooling time and the observed peak in the EM from *GOES*. At the end of the dominant conductive cooling phase III, the plasma temperature has dropped to 13.4 MK. This corresponds to a cooling rate of ~14,300 K s^{-1}. Conductive cooling does not dominate the evolution of the cooling loop at all temperatures. At the end of phase III, the observed EM reaches a peak (as expected) and, assuming the emitting volume has not changed significantly within 2 minutes, then the electron density will have increased to 3.5×10^{10} cm^{-3}. Consequently, there will be an increase in radiative losses and eventually a transition to predominantly radiative cooling, as the loop temperature decreases and the loop density increases (Antiochos & Sturrock 1976; Cargill 1994).

5.2. Dominance of Radiative Cooling

The efficiency of conductive cooling decreases with the temperature drop-off while the efficiency of radiative cooling increases, and we enter phase IV, following Reale (2007). The EM can be approximated as a power law of the form EM $\sim T^b$ (Dere & Mason 1993; Brosius et al. 1996; Winebarger et al. 2011). We fit a power law with an index b of 3.6 to this curve, which is indeed characteristic of strong heating events such as flares. Next, we consider radiative cooling timescales (τ_r) from the Cargill model and compare with the observations. The radiative cooling timescale can be calculated from Equation (4) through neglecting heating, conductive losses, and energy transport due to flow terms, resulting (Cargill et al. 1995) in

$$n_e^{\zeta}\,\chi\,T^{\alpha} = \frac{k_{\rm B}}{\gamma - 1}\,n_e\,\frac{\partial T}{\partial t}. \tag{7}$$

After rearranging the terms and integrating, we can express the radiative cooling timescale as

$$\tau_r = \frac{k_{\rm B}}{(\gamma - 1)(1 - \alpha)\chi}\,\frac{T^{1-\alpha}}{n_e^{\zeta - 1}}. \tag{8}$$

In the limit 10^6–10^7 K, we expect that $\zeta = 2$, $\chi = 1.2 \times 10^{-19}$, $\alpha = -1/2$, and $\gamma = 5/3$ according to Rosner et al. (1978), and after inputting the same plasma

temperature and density properties at 15:46:32 UT (the start of the dominant radiative cooling phase IV), we calculate a radiative cooling timescale of ~4764 s (or ~1 hr 20 minutes), which is much longer than the expected radiative cooling timescale from observation (where 26 minutes after the temperature peak, we have the first appearance of the chromospheric component of coronal rain). We do not assume that there are discrete start and end times with respect to the dominance of radiative cooling versus conductive cooling, but these time estimates give a good indication of approximately when we can expect to detect such a transition. Similarly, Raftery et al. (2009) investigated a C-class flare and also found values for τ_c (300 s) to be much less than τ_r (~4000 s), which may indicate that for relatively weak C-class flares we may not expect a large conductive cooling timescale given that the peak temperatures will be relatively low. A comparison was made between the Cargill approach and the enthalpy-based thermal evolution of loops (EBTEL) model (Klimchuk et al. 2008) during the flare cooling phase. EBTEL simultaneously calculates the conductive and radiative losses throughout the flare and estimates the onset time at which one energy transfer mechanism dominates over the other. In a comparison between the Cargill model and EBTEL, it was shown by Raftery et al. (2009) that both models were in agreement with respect to the predicted time (τ_*) at which radiative losses dominate over conductive losses. According to the Cargill model, the time at which the dominant cooling mechanism changes from conductive to radiative cooling (τ_*) can be defined as the ratio of the respective timescales (Cargill et al. 1995) as

$$\tau_* = \tau_{c_0}\left[\left(\frac{\tau_{r_0}}{\tau_{c_0}}\right)^{7/12} - 1\right], \quad (9)$$

where the subscript "0" denotes the initial values of the conductive cooling timescale at the start of the cooling phase (τ_{c_0}) and the radiative cooling timescale at the start of the radiative phase (τ_{r_0}). The time τ_* at which $\tau_{c_0} \approx \tau_{r_0}$, that is, when the dominant loss mechanism switches from conduction to radiation (Cargill & Klimchuk 2004), is 913 s, which corresponds to ~15:59:42 UT, as marked with a vertical dashed line in Figure 20. The predicted temperature from the start of the cooling phase, which is expected at τ_*, is given (Cargill et al. 1995) as

$$T_* = T_0\left(\frac{\tau_{r_0}}{\tau_{c_0}}\right)^{-1/6}. \quad (10)$$

Here we expect the temperature of the plasma in the flare loop to have cooled to 8.4 MK. The observed temperature at τ_* from Figure 20 is in the range of 6–7 MK. Indeed, the Cargill model makes an accurate approximation in this regard. According to Cargill et al. (1995), if $\tau_{c_0} \ll \tau_{r_0}$, then the total loop cooling time ($\tau_{\rm cool}$), assuming conductive cooling is evaporative rather than static, can be approximated as

$$\tau_{\rm cool} \approx \frac{5}{3}(\tau_{r_0}^{7/12}\tau_{c_0}^{5/12}). \quad (11)$$

Here we calculate the total loop cooling time as 1,848 s, which corresponds to an end time of ~16:15 UT. We detect cool, dense chromospheric components in the coronal rain formation, initially at the loop top, at 16:10:19 UT, which is clearly earlier than the predicted time. The measured densities may be larger than what is reported here, as a result of overestimating the volume of the emitting plasma, which would lead to reduced radiative cooling timescales in the later phases of cooling (Reale & Landi 2012). From the averaged red line in Figure 20 (which extends from the temperature peak to the formation of cool, dense chromospheric rain clumps within phase V), the temperature drop throughout phase IV corresponds to a cooling rate of 7300 K s^{-1}. Next, we consider the properties of the loop cooling into the EUV coronal and TR plasma, using the AIA DEM calculations. From Figure 20, we detect a significant steepening of the temperature decrease from phase IV into phase V, which we class as catastrophic cooling that commences prior to the first appearance of the chromospheric rain component. With the red curve we estimate an acceleration in the rate of cooling of the plasma reaching a maximum at 22,700 K s^{-1} between frames no. 86 and 88. This apparent acceleration in the cooling is marked as phase V in Figure 20, and changes in the properties of the cooling plasma during this phase will give valuable insight into the nature of *catastrophic cooling*.

5.3. Transition from Radiative Cooling to Catastrophic Cooling and Rain Flows

The sequential appearance of the formation of coronal rain from the EUV, visible, and near-IR passbands is imaged and indicates a rapid progression of the plasma temperature through these passbands, as presented in Figures 11–13. In Figure 18, we presented the DEM versus temperature profiles in order to understand the nature of the plasma temperature and density properties immediately prior to the onset of catastrophic cooling and at the location of the rain formation. So far we have considered the role of conductive and radiative cooling in the early phases of the decay of the flare. At later stages, energy transport in mass flows could come from enthalpy-based cooling (i.e., enthalpy flux). Even though enthalpy flux removes energy from the corona in mass flows, it is not an energy-loss mechanism like radiation, but rather it redistributes energy from the corona to the TR (Bradshaw & Cargill 2010).

Whenever the radiative cooling mechanism becomes dominant, loop depletion starts very slowly at first and then becomes progressively faster since the pressure decrease can no longer support the condensing plasma (Reale 2007). In this scenario, entalpy-based radiative cooling may play an important role in sustaining the TR radiative losses through a redistribution of the energy driven by downflows. Bradshaw (2008) demonstrated that for certain flow velocities the enthalpy flux (mechanical transport of energy) could balance the radiative energy loss in cooling active-region loops in order to avoid catastrophic cooling and, in turn, power the TR radiation. According to Bradshaw (2008), the critical velocity that the downflow must reach in order to drive an enthalpy flux sufficient to sustain the TR radiative emission and avoid catastrophic loop drainage is in the range of 15.3–76 km s^{-1} along the loop leg (close in height to the TR) for loop densities in the range of 1–5 $\times$ 10^{10} cm^{-3} when the loop apex is 1 MK. Mass transport associated with the cooling loop in this study is clearly present in the EUV for coronal plasma, as well as the TR plasma at the end of phase IV and start of phase V when the loop temperature is expected to be between $10^{5.9}$ K and $10^{6.2}$ MK (see red curve at start of phase V in Figures 20 and 19 bottom row). Between frames no. 86 and 88, corresponding to 35 s into phase V, we detect the evolution

from coronal plasma temperatures (>1.5 MK) to radiative losses in the TR plasma (~0.5 MK) in the DEM profiles localized to the loop-top sources of coronal rain. After this short interval, we detect catastrophic loop drainage originating at the loop top in multithermal mass flows, before appearing in the loop legs, where we detect apparent velocities of ~54.5 km s^{-1} (see Figure 8). Furthermore, we have calculated the densities in the flare loop of ~3.5×10^{10} cm^{-3}; therefore, according to Bradshaw (2008), we should expect that the enthalpy flux will balance the TR radiative losses in the loop leg. Indeed, during this period of enthalpy flux in the loop leg, we detect the increased radiative emission signature of a loop in the TR plasma in the DEM maps at 16:12:23 UT with temperatures of $10^{5.8}$ K (see Figure 17 top right panel) where we detect the Hα flows. This cospatial, multithermal flow field development leading to bright TR emission signatures along the loop leg between 16:10:59 UT and 16:13:22 UT is presented in detail in Figure 13. This loop exists at TR plasma temperatures for as long as the high-speed mass flows are present, as the enthalpy-based cooling model predicts.

Despite this, we find that catastrophic cooling to chromospheric temperatures at the loop-top source specifically has rapidly surpassed the mechanism of enthalpy flux in powering the TR losses, originally proposed to prevent collapse and extensive loop depletion. In other words, we have rapid loop-top catastrophic cooling, followed by multithermal mass flows, leading to loop-leg enthalpy flux to power the TR radiative losses. This outcome is somewhat supported by Cargill & Bradshaw (2013), who compared analytical models with numerical results to show that catastrophic cooling is due to the inability of a loop to sustain radiative or enthalpy cooling below a critical temperature, which can be >1 MK in flares. It may be interpreted that the enthalpy flux in mass flows at the loop apex cannot be expected to be as sufficient as along the loop leg in sustaining the enthalpy-based radiative cooling process, thereby enabling accelerated cooling at the apex.

Next, we investigate the observed catastrophic cooling phase in more detail, using the temperature and DEM changes within Figure 19 to estimate local changes in the plasma density of the chromospheric component of the rain source, in order to better characterize the onset of catastrophic cooling observed here with respect to the analytical and numerical models of Reale & Landi (2012), Bradshaw & Cargill (2010), and Cargill & Bradshaw (2013).

5.4. Plasma Properties during Catastrophic Cooling

The DEM profiles presented in this analysis (see Figure 18 bottom row), between 16:09:44 UT and 16:10:59 UT, reveal important information regarding the TR plasma properties during catastrophic cooling. Assuming that we have a multithermal rain structure forming cospatially at the loop-top source and assuming the volume of the emitting region as a sphere with the diameter of the contoured region centered (for the longest diagonal) on the rain-formation region (see the 30.4 nm black contour at 16:10:04 UT in Figure 11), then we can calculate the density of the TR plasma component from the DEM locally at the source of the rain. From this estimate, we can momentarily infer the density of the Hα chromospheric component by deducing an ideal gas pressure balance across the structure whereby the rain source has a hotter outer sheath of TR plasma coating a cooler and more dense core in emission at 16:10:19 UT in Hα (see Figure 11). It is important to note that this determination of plasma properties from the DEM will represent a lower limit to the density of the rain strands before loop depletion, given that condensation will continue to increase the plasma density locally, until it is observed in absorption in Hα and proceeds to flow along the loop legs. Through considering the DEM in the range of $5.5 < \mathrm{Log}_{10}\, T < 5.7$ between 16:09:44 UT and 16:10:59 UT (see Figure 18 bottom row), we notice a significant increase due to the appearance of the rain source, and we calculate the EM by integrating the DEM curve across this temperature range as follows:

$$\int_{5.5}^{5.7} \xi(T)dT = EM. \tag{12}$$

Therefore, assuming a diameter of 1 arcsec for the emitting region (corresponding to the area of the five pixels in the black cross in Figure 18) used to generate the DEM, we estimate an emitting volume of 3.28×10^{22} cm^3. As a result, the electron density at the loop-top source in the TR plasma varies between 7.45×10^9 cm^{-3} and 1.10×10^{10} cm^{-3} comparing between changes in the profiles at 16:09:44 UT and 16:10:59 UT, that is, around the time of the chromospheric rain formation. The densities that we calculate are representative of the EUV component of the plasma, and we fully expect the eventual chromospheric component to have a much higher density (as demonstrated in Antolin et al. 2015). Assuming a momentary pressure balance in the loop-top source, before the onset of the multithermal flow along the loop legs away from the loop top at frame 16:10:59 UT (see Figure 12), we can estimate the density of the Hα component with a gas temperature of ~22,000 K from Figure 6. Equating the ideal gas law, we estimate the density of the chromospheric component of coronal rain in this time range to be $9.21 \times 10^{11} \pm 1.76 \times 10^{11}$ cm^{-3}. In the chromospheric component of the coronal rain, we detect a range of cross-sectional widths of rain clumps in the range of 100–200 km within Hα images across the EUV loop (refer to Scullion et al. 2014 for more information), amounting to eight parallel strands. Using the rain strand widths as a lower limit to the volume of the cooling strands, together with the electron densities estimated here from the chromospheric plasma, we calculate the mass loss rate from the postflare arcade to be as much as $1.98 \times 10^{12} \pm 4.95 \times 10^{11}$ g s^{-1}.

As the plasma continues to cool below 1–2 MK in flare loops, one must consider the shape of the optically thin loss function. When we consider again the radiative loss timescale using the Rosner et al. (1978) radiative loss scaling law (for optically thin plasma) in the range of $10^{5.7}$–$10^{6.3}$ K (i.e., the lowest temperature range below which the plasma is assumed to be optically thick), we change the expression for the radiative cooling timescale to

$$\tau_r = 3 \times 10^{21.94} \frac{k_B\, T}{n_e}. \tag{13}$$

The near-simultaneous and parallel-forming rain clumps might be explained by a very short radiative loss timescale in individual strands, arising from modifications to the scaling law in the different temperature regimes, resulting in a more rapid temperature decline with a relatively small change in density. For the derived TR plasma densities at the time of chromospheric rain formation and a plasma temperature of $\mathrm{Log}_{10}\, T = 5.9$, which matches the expected temperature from the red curve of Figure 20, we calculate a new radiative cooling

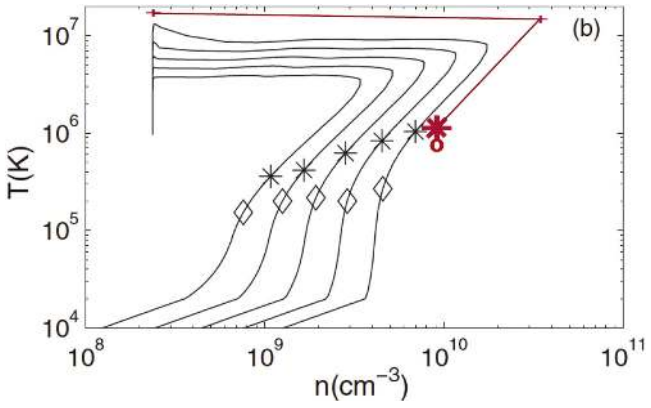

Figure 21. This figure is extracted from Cargill & Bradshaw (2013) (Figure 1 (b)), and the black curves describe the relation between the average temperature and density for five loops that were previously discussed as numerical simulation runs 6–10 in Bradshaw & Cargill (2010). Time increases as each curve is followed in a clockwise direction. The group of five loops have lengths ($2L$) in the range 67–72 Mm. The black stars and diamonds show the start and end of the transition to catastrophic cooling according to the model. The red star corresponds to the temperature and density at the start of catastrophic cooling from the observations, to compare with the corresponding simulated black stars. The red crosses mark the temperature and density at the EM/density peak from the observations, to compare with the corresponding density peak of the simulated black curves. The red circle corresponds to the analytical solution for the critical temperature for the onset of catastrophic cooling (T_c) from Equation (15).

timescale of 2–3 minutes, which continues to be greater than the expected or observed timescale. So far we have attempted to characterize the flare loop cooling processes for this event using simplified model assumptions that have largely proved very accurate, although the model consistently predicts longer total loop cooling times than observed in this flare.

Reale & Landi (2012) modeled radiative loss functions derived from the recent CHIANTI database (Landi et al. 2012). They found relatively "faster" onset of catastrophic cooling in loops, thereby reducing the total loop cooling time, resulting in the plasma temperature dropping below 10^5 K in tens of seconds. This is thought to be attributed to a factor of four increase in the coronal radiative losses in the latest model when compared with Rosner et al. (1978). Furthermore, the flare loop temperature and density properties at the start of the radiative cooling phase described here are highly comparable with case 1 from Reale & Landi (2012), as presented in Cargill & Bradshaw (2013) Table 1, which suggests that the critical temperature for catastrophic cooling will be in the range of $10^{6.0}$–$10^{6.2}$ K. As mentioned previously, we expect the start of catastrophic cooling occurs in the TR/low corona plasma with at least $10^{5.9}$–$10^{6.2}$ K in temperature. Furthermore, we have shown that an earlier onset of catastrophic cooling is taking place, and it appears within the range of 35–124 s after the plasma has cooled into the 1.5–7 MK coronal temperatures.

Numerical models describing the cycle of cooling of flare loops can be represented using n_e–T diagrams (Jakimiec et al. 1992). The density versus temperature variations for a group of five loops was originally presented in Bradshaw & Cargill (2010) (their Table 1, runs 6–10) and extracted from Cargill & Bradshaw (2013) (their Figure 1(b)) and are now presented here in Figure 21. We present this figure in order to place our measurements in the context of flare models that accurately take into account the late process of catastrophic cooling and loop depletion. In Figure 21, the temperature and density ranges estimated from the observations, corresponding to the loop-top rain source at the onset of catastrophic cooling, are marked with a red star. Likewise, the temperature and density ranges estimated for the start of the radiative cooling phase IV are marked with a red cross. The loop lengths for the simulation runs (black curves) increase from left to right but vary by as much as 6% and are comparable with the loop length from our observations. Comparing the runs from right to left, each loop has a sequentially larger volumetric heating rate, so the radiative cooling starts with sequentially higher temperatures and densities. The volumetric heating rate almost doubles for each loop, increasing from 5.31×10^{-3} erg cm^{-2} s^{-1} (left-most curve) to 8.5×10^{-3} erg cm^{-2} s^{-1} (right-most curve). It is clear that the observations presented (directly connected by the red line) may well represent the next "class" of loop in this particular grouping, which would correspond to a loop that has been volumetrically heated (during phase I), by as much as 17.0×10^{-3} erg cm^{-2} s^{-1}, that is, if the trend is indeed linear.

We also find a strong agreement between the starting temperature of the simulated catastrophic cooling phase (marked by the black stars) and the observed starting temperature range of catastrophic cooling from the observations (red star). The red circle in Figure 21 marks the analytical solution for the critical temperature defining the commencement of catastrophic cooling, which is again in very good agreement with the observations here, as it is with the numerical models outlined in detail in Cargill & Bradshaw (2013). What this means is that the onset of catastrophic cooling can indeed begin in the coronal plasma and very quickly accelerate through the TR passbands to chromospheric temperatures without a significant change in density. Furthermore, the previous discrepancy between the analytical total loop cooling time and observed total loop cooling time is now more closely matched, and this discrepancy is also acknowledged in Cargill & Bradshaw (2013). Importantly, in the case of relatively short, hot flaring loops, the model predicts that we can expect catastrophic cooling to commence at ~1 MK, as our observations indicate. With a valid model comparison with our observations, how can the model inform the observations regarding the origin of catastrophic cooling leading to coronal rain at the loop top?

It is considered that after the plasma is evaporated from the chromosphere, along each loop leg, the resulting compression near the loop top could generate slow-mode acoustic waves. In Cargill & Bradshaw (2013), the definition for the critical temperature describing the onset of catastrophic cooling suggests an important role in the propagation of such sound waves in cooling loops, and this process manifests itself in the ratio between the sound travel time and the radiative cooling time. These sound waves may transport and redistribute a substantial amount of energy and dictate the relative importance of pure radiative cooling over enthalpy-based radiative cooling, which balances the losses and sustains cooling. Cargill & Bradshaw (2013) have shown that when the $T \sim n$ scaling in the loop cooling starts to break down, then the temperature at which this happens defines the onset of catastrophic cooling. A new scaling dependency appears as $T \sim n^{\delta}$, where δ is typically 2 for short loops but can reduce to 1 for long loops and is determined by the relative importance of the coronal radiative losses to the enthalpy flux (Bradshaw & Cargill 2010). Larger δ values indicate the dominance of radiation with small coronal mass loss, whereas smaller values

indicate the dominance of enthalpy and a relatively large coronal mass loss (Bradshaw & Cargill 2005). Cargill & Bradshaw (2013) state that the downflow required by enthalpy flux continually adjusts through sound waves that will sufficiently maintain the $T \sim n$ relationship, provided the radiative cooling time in the corona (τ_r) is greater than the sound travel time (τ_s). Since sound wave travel time is determined by the loop length and sound speed, loop length and loop temperature will also limit the expected onset of catastrophic cooling, aside from the volumetric heating rate of the flare. The sound travel time is therefore defined as

$$\tau_s = \frac{L}{C_s} \tag{14}$$

where the isothermal sound speed $C_s = (2k_B T/m_p)^{1/2}$ for an electron–proton plasma, and m_p is the proton mass. When $\tau_r \leqslant \tau_s$, enthalpy-based radiative cooling stops and the loop cools predominantly by radiation, leading to catastrophic cooling. After equating these timescales and taking the conditions describing the start of the radiative cooling phase with subscript "0" (i.e., using τ_{r0} and $\tau_{s0} = 68$ s), Cargill & Bradshaw (2013) derived a general expression for the critical temperature (T_c) for the onset of catastrophic cooling as

$$T_c = T_0 (\tau_{s0}/\tau_{r0})^{\frac{3}{2}-\delta-\frac{1}{\alpha}}. \tag{15}$$

From Bradshaw & Cargill (2010), it is shown in Table 2 that for simulation runs 6–10 (corresponding to loops right to left in Figure 21) the value for δ generally decreases relatively linearly from 1.94 to 1.79. If the observations assigned to Figure 21 indeed correspond to the next "class" of model parameters, then given the parallels between the red line connecting the red symbols and the adjacent black curves, we could expect that the value for δ might equally scale up, so it should be greater than 1.94 and very close to 2.0. Therefore, from the conditions at the loop-top source at the end of phase IV, with large δ we expect radiative cooling to dominate over enthalpy-based radiative cooling. After substituting into this expression our estimations for the temperature, radiative cooling timescale, and sound travel timescale and with $\alpha = -1/2$, we determined the critical temperature of 0.78 MK (i.e., $10^{5.8}$ K). This is marked in Figure 21 with the red circle and is in good agreement with the onset of steep gradients in the temperature profile described by the red curve in Figure 20 at the transition to phase V, at $10^{5.9}$–$10^{6.2}$ K.

This analysis suggests that at the loop apex, where we do not expect strong flows (compared with loop legs), the radiation cooling should dominate, and the model suggests it does. This leads to a runaway cooling process for hot, short loops (with a relatively short sound travel timescale), leading to catastrophic cooling at temperatures of around ~1–1.5 MK in flares, which is in close agreement with these observations. If the sound waves cannot sustain the coronal radiative losses, then catastrophic cooling is initiated, and quickly the local temperature drops to chromospheric levels within tens of seconds and we have rain flows in Hα. One interesting correlation is the similarity between τ_s, which is 68 s, and the periodicity in the Hα rain flows of 55–70 s along a given loop trajectory (see Figure 7). On this point, one hypothesis is that possibly the incident rain flows from the loop top are triggering plasma compressions between the substrands, that is, compressions within the coronal/TR medium of the loop arcade system, triggering new sound or acoustic wave propagation in their wake. At which point, the waves continue to replenish the energy balance requirements of the coronal and TR radiative losses for another 68 s, until the condition for catastrophic cooling is met again, leading to further pressure balancing, accretion, and loop drainage in the new Hα rain clump. That cyclic behavior between the dominance of radiative and enthalpy-based radiative cooling might account for the sequential formation of rain flows in the loop system. Therefore, one might expect a linear relationship between sequential rain formation period and loop length at constant density. Furthermore, strong acoustic waves have been predicted for short heat pulses in flare loop models on the period of a few minutes (Reale 2016), which might account for the fluctuations in the *GOES* EM, as shown in Figure 20.

5.5. Fine-scale Structure in Coronal Loops

The Cargill model accounts for this acceleration in the loop cooling time in one such loop strand (with 0D assumptions). However, we observe multiple parallel strands of rain flows within the loop system. If successive chromospheric rain strands can form in parallel, each independently cooling catastrophically, then this model will be well suited to studying rain formation in postflare arcades collectively. This scenario may be plausible given that we can already identify multiple independent coronal rain formation sites at the loop top from the Hα temperature maps (see Figure 6). Each of these may correspond to a unique strand within the loop system independently cooling and yielding rain flows. Reale et al. (2012) showed that if a bundle of subloops (strands in this case) is assumed to be heated at slightly different times, then they could obtain a closer match between the observed and modeled light curves for plasma below 2 MK in flare arcades. A future statistical study of the individual rain strands formed throughout this loop system and their associated DEM properties may yield further insight into the possibility of a collective convolution of coolings, and the net effect on the estimated timescales for cooling may adjust slightly. Indeed, we find some evidence that chromospheric rain clumps in the loop arcade can form at slightly different times, and they can even appear periodically (see Figure 7), indicating some underlying physics connecting the formation of successive parallel clumps of rain. The multistranded nature of coronal rain may not be entirely thermally isolated, and there could be energy transfer between adjacent strands as a result of sympathetic cooling, which has been demonstrated numerically in the case of quiescent coronal rain formation, leading to parallel rain strand formation (Fang et al. 2013). The transport of thermal energy via the MHD thermal mode (also known as the entropy mode in the absence of thermal conduction) was first predicted by Field (1965) between parallel strands and cannot be ruled out in having a role in accelerating the cooling process. The generation of this thermal wave is guaranteed by the small but nonzero perpendicular thermal conduction in the corona. The spatial distribution of such mode, across a set of magnetic field lines, results in a set of dense rain clump formations with multiple smaller clumps located beside each other and of similar widths. This process will require further investigation with more sophisticated, multistranded models of cooling loops to determine the impact of the thermal mode with respect to the formation of adjacent coronal rain clumps (Antolin et al. 2015).

In general, it is most likely that the structure of the postflare arcades is composed of a bunch or bunches of loop strands,

rather than a single strand, and the approximations here are based on single-strand models. Kontar & Jeffrey (2010) and Kontar et al. (2010) use *RHESSI* observations of sources of X-ray emission during flaring to show that a chromospheric density model involving multiple density threads can explain both the position of the maximum and the vertical size of the sources. Likewise, Reale et al. (2012) found a correlation with *SOHO*/SUMER (Wilhelm et al. 1997) spectral lines under flaring conditions when they assumed a model of flare heating within a bundle of subloops of equal length. A multistranded model will be important to consider if we only focused on the *GOES* X-ray data or our analysis involved studying the loops in their entirety in the EUV or visible or near-IR wavelengths. If we wanted to draw conclusions about the nature of the loop in its entirety, then we should consider the convolution of cooling of the individual strands in the bunch and the filling factor associated with flaring plasma in the arcades. On that point, we should not expect that all substrands of the postflare loop system are 100% filled with heated plasma, all at the same time, during the flare impulsive phase. Instead, here we focus on deducing plasma properties of the loop-top coronal rain formation region that composes part of a single chromospheric coronal rain strand within a small region of the entire multithermal loop system (see Figures 4, 11, and 14). In summary, the application of single-strand model assumptions in our timescale analysis of the formation of submillion kelvin rain is valid.

It is important to note that the cooling timescales calculated are only applicable to the linear regime, and catastrophic cooling is a nonlinear effect. We emphasize that the plasma properties determined here correspond to hotter components of the multithermal rain sources and not the final product, that is, not the chromospheric component of the rain that is optically thick. Indeed, continually increasing densities in the cooling plasma will also shorten the ionization and recombination timescales and allow the plasma to efficiently adjust its ionization status (Golub et al. 1989); in other words, the plasma should respond quickly to the rapidly changing conditions. Furthermore, it is important to state that we still need to confirm whether the observed radiative cooling rates can continue down the low (submillion kelvin) temperature bins, given the rates of condensation leading to optically thick chromospheric plasma, since the reduced efficiency of radiative losses within an optically thick plasma in a coronal loop-top environment may not account for such a rapid cooling timescale alone. Hence, based on this study, we do not know whether or not we still need extra mechanisms, such as the MHD thermal mode, in order to explain catastrophic cooling into the chromospheric component of the rain in flaring conditions or in the case of quiescent coronal rain. Considering these effects on the measurements deduced in this study, together with the inherent uncertainties in the measurement of densities from observation of the DEMs, leads us to reiterate that the reported timescales and the expected density enhancement in the chromospheric component of the flare-driven coronal rain will vary by a few factors.

6. CONCLUSIONS

We investigate in detail and at the highest resolution a "textbook" example of the flare loop cooling process from the start of the decay at a temperature peak of 15.4 MK in the X-ray channels with *GOES*, through the EUV channels of the EUV corona and TR with AIA, finishing as mass condensations at chromospheric temperatures in the visible and near-IR with CRISP. In doing so, we reveal the chromosphere–corona mass cycle from the source, as bright Hα ribbons, to sink, as coronal rain. We detect five phases that characterize the postflare loop dynamics: heating, evaporation, conductive cooling dominance for 122 s, radiative/enthalpy-based cooling dominance (<4700 s), and finally catastrophic cooling at a critical plasma temperature close to $10^{5.8}$ K. In summary, we find an excellent agreement between the observations and analytical model predictions in all phases, primarily derived in Cargill et al. (1995) and Cargill & Bradshaw (2013), which very much agree with respect to the timescales associated with the dominant cooling processes, as well as the critical temperature for the onset of catastrophic cooling.

We discover that, during catastrophic cooling of phase V, the plasma cools at a maximum rate of 22,700 K s^{-1} in multiple loop-top sources, and this presents itself as a catastrophic loop depletion in up to eight parallel strands. If successive chromospheric rain strands can form in parallel, each independently cooling catastrophically, then the Cargill model will be well suited to studying rain formation in multistranded postflare arcades. The acceleration in the rate of cooling to chromospheric temperatures is evidence for a catastrophic cooling process. The plasma can undergo catastrophic cooling from ~1 MK to ~22,000 K in tens of seconds (specifically 35–124 s here) rather than in many minutes as with quiescent coronal rain, which is remarkably fast. This could be explained by the fact that the flaring process leads to substantially larger mass loading of the coronal loop system, leading to shorter radiative cooling timescales.

We study the initial rain-formation region at the loop apex in detail, and we find strong evidence to suggest the presence of a multithermal flow within flare-driven coronal rain strands. From spatial correlation and tracking of the flows from the loop top along the legs, between the emitting regions in the EUV and chromospheric channels, we could identify the multithermal structure of the rain flows. Then with a DEM analysis, employing a novel regularized inversion code, we calculated the density of the EUV plasma from the emitting volume (estimated from the FOV). Assuming a pressure balance across the multithermal structure of the rain clump at the formation of the rain source at the loop top, we estimated the density of the chromospheric component of the rain to be $9.21 \times 10^{11} \pm 1.76 \times 10^{11}$ cm^{-3}, which is characteristic of quiescent coronal rain densities, as reported by Antolin et al. (2015). Using the rain strand widths, in the range of 100–200 km in cross section, together with the electron densities estimated here from chromospheric plasma, we calculate the mass loss rate from the postflare arcade to be as much as $1.98 \times 10^{12} \pm 4.95 \times 10^{11}$ g s^{-1}.

We detect catastrophic cooling at the loop-top source initially, followed by multithermal rain flows along the loop leg, leading to a notable increase in the TR EM at $10^{5.8}$ K from the DEM maps for the loop leg. Model predictions for the loop-top temperature and density properties ascribe to a downflow velocity in the loop leg the same magnitude that is observed (i.e., 54.5 ± 2 km s^{-1}), suggesting a redistribution of the energy balance in the loop during the flow and a dominance of the enthalpy flux in powering the TR emission. We also detect a deceleration in the rain flow closer to the loop footpoint from 76 to 60 m s^{-2}, which is consistent with numerical

simulation of rain flows into a more dense medium of the TR and chromosphere. The role of enthalpy flux in sustaining the TR losses may play a similar role in sustaining the corona losses, and the balance between enthalpy-based radiative cooling and unsustained radiative cooling dictates the onset of catastrophic cooling. What drives the transition to catastrophic cooling is the sound wave travel time according to Cargill et al. (1995). We reveal a close proximity between the model predictions (of $10^{5.8}$ K) and the observed properties (between $10^{5.9}$ and $10^{6.2}$ K) defining the temperature onset of catastrophic cooling. This suggests that the role of sound waves in loops, through sustaining the enthalpy flux, may be important when determining the eventual onset of Hα rain formation.

Finally, we postulate that the ratio between radiative cooling timescales and sound wave travel timescale may not only be important in calculating the critical temperature for the onset of catastrophic cooling and coronal rain formation in flares but in explaining the origin of the periodicity between rain clumps, which is 68 s and is on the order of the sound wave travel time calculated here. Future work will focus on understanding the energy balance between interacting loop strands collectively and the physics associated with the formation of parallel adjacent rain flows in postflare arcades.

The authors are most grateful to the staff of the *SST* for their invaluable support with the observations. The Swedish 1 m Solar Telescope is operated on the island of La Palma by the Institute for Solar Physics at Stockholm University in the Spanish Observatorio del Roque de los Muchachos of the Instituto de Astrofísica de Canarias. E.S. is a Government of Ireland Postdoctoral Research Fellow supported by the Irish Research Council. E.S. would like to acknowledge the DJEI/DES/SFI/HEA Irish Centre for High-End Computing (ICHEC) for the provision of computational facilities (in particular the FIONN cluster) and support. E.P.K. was supported by STFC. E.S. would like to acknowledge the support from the International Space Science Institute, Bern, Switzerland and to the International Team involved in the project "Implications for coronal heating and magnetic fields from coronal rain observations and modeling" lead by P.A. G.V. is funded by the European Research Council under the European Union's Seventh Framework Programme (FP7/2007-2013)/ERC grant agreement no. 291058. SW acknowledges support by the Research Council of Norway (grant 221767/F20).

REFERENCES

Ahn, K., Chae, J., Cho, K.-S., et al. 2014, SoPh, 289, 4117
Antiochos, S. K., & Klimchuk, J. A. 1991, ApJ, 378, 372
Antiochos, S. K., MacNeice, P. J., Spicer, D. S., & Klimchuk, J. A. 1999, ApJ, 512, 985
Antiochos, S. K., & Sturrock, P. A. 1976, SoPh, 49, 359
Antiochos, S. K., & Sturrock, P. A. 1978, ApJ, 220, 1137
Antolin, P., & Rouppe van der Voort, L. 2012, ApJ, 745, 152
Antolin, P., Shibata, K., & Vissers, G. 2010, ApJ, 716, 154
Antolin, P., Vissers, G., Pereira, T. M. D., Rouppe van der Voort, L., & Scullion, E. 2015, ApJ, 806, 81
Aschwanden, M. J., & Boerner, P. 2011, ApJ, 732, 81
Battaglia, M., Kleint, L., Krucker, S., & Graham, D. 2015, ApJ, 813, 113
Bradshaw, S. J. 2008, A&A, 486, L5
Bradshaw, S. J., & Cargill, P. J. 2005, A&A, 437, 311
Bradshaw, S. J., & Cargill, P. J. 2010, ApJ, 717, 163
Brosius, J. W. 2003, ApJ, 586, 1417
Brosius, J. W., Davila, J. M., Thomas, R. J., & Monsignori-Fossi, B. C. 1996, ApJS, 106, 143
Cargill, P. J. 1993, SoPh, 147, 263
Cargill, P. J. 1994, ApJ, 422, 381
Cargill, P. J., & Bradshaw, S. J. 2013, ApJ, 772, 40
Cargill, P. J., & Klimchuk, J. A. 2004, ApJ, 605, 911
Cargill, P. J., Mariska, J. T., & Antiochos, S. K. 1995, ApJ, 439, 1034
de la Cruz Rodríguez, J., Löfdahl, M. G., Sütterlin, P., Hillberg, T., & Rouppe van der Voort, L. 2015, A&A, 573, A40
Dere, K. P., Landi, E., Mason, H. E., Monsignori Fossi, B. C., & Young, P. R. 1997, A&AS, 125, 149
Dere, K. P., & Mason, H. E. 1993, SoPh, 144, 217
Doschek, G. A., Boris, J. P., Cheng, C. C., Mariska, J. T., & Oran, E. S. 1982, ApJ, 258, 373
Doschek, G. A., Cheng, C. C., Oran, E. S., Boris, J. P., & Mariska, J. T. 1983, ApJ, 265, 1103
Fang, X., Xia, C., & Keppens, R. 2013, ApJL, 771, L29
Feldman, U., Landi, E., & Curdt, W. 2003, ApJ, 585, 1087
Field, G. B. 1965, ApJ, 142, 531
Fisher, G. H., Canfield, R. C., & McClymont, A. N. 1985, ApJ, 289, 425
Foukal, P. V. 1976, ApJ, 210, 575
Foullon, C., Verwichte, E., Nakariakov, V. M., Nykyri, K., & Farrugia, C. J. 2011, ApJL, 729, L8
Froment, C., Auchère, F., Bocchialini, K., et al. 2015, ApJ, 807, 158
Goldsmith, D. W. 1971, SoPh, 19, 86
Golub, L., Hartquist, T. W., & Quillen, A. C. 1989, SoPh, 122, 245
Hannah, I. G., & Kontar, E. P. 2012, A&A, 539, A146
Henriques, V. M. J. 2012, A&A, 548, A114
Hildner, E. 1974, SoPh, 35, 123
Jakimiec, J., Sylwester, B., Sylwester, J., et al. 1992, A&A, 253, 269
Karpen, J. T., Antiochos, S. K., Hohensee, M., Klimchuk, J. A., & MacNeice, P. J. 2001, ApJL, 553, L85
Kawaguchi, I. 1970, PASJ, 22, 405
Klimchuk, J. A. 2006, SoPh, 234, 41
Klimchuk, J. A., Patsourakos, S., & Cargill, P. J. 2008, ApJ, 682, 1351
Kontar, E. P., Hannah, I. G., Jeffrey, N. L. S., & Battaglia, M. 2010, ApJ, 717, 250
Kontar, E. P., & Jeffrey, N. L. S. 2010, A&A, 513, L2
Kontar, E. P., & MacKinnon, A. L. 2005, SoPh, 227, 299
Kontar, E. P., Piana, M., Massone, A. M., Emslie, A. G., & Brown, J. C. 2004, SoPh, 225, 293
Kopp, R. A., & Pneuman, G. W. 1976, SoPh, 50, 85
Landi, E., Del Zanna, G., Young, P. R., Dere, K. P., & Mason, H. E. 2012, ApJ, 744, 99
Landi, E., Landini, M., Dere, K. P., Young, P. R., & Mason, H. E. 1999, A&AS, 135, 339
Lemen, J. R., Title, A. M., Akin, D. J., et al. 2012, SoPh, 275, 17
Leroy, J.-L. 1972, SoPh, 25, 413
Levine, R. H., & Withbroe, G. L. 1977, SoPh, 51, 83
Martínez Oliveros, J.-C., Krucker, S., Hudson, H. S., et al. 2014, ApJL, 780, L28
Mendoza-Briceño, C. A., Sigalotti, L. D. G., & Erdélyi, R. 2005, ApJ, 624, 1080
Milligan, R. O., Gallagher, P. T., Mathioudakis, M., et al. 2006a, ApJL, 638, L117
Milligan, R. O., Gallagher, P. T., Mathioudakis, M., & Keenan, F. P. 2006b, ApJL, 642, L169
Moore, R. L., & Datlowe, D. W. 1975, SoPh, 43, 189
Müller, D. A. N., Peter, H., & Hansteen, V. H. 2004, A&A, 424, 289
O'Shea, E., Banerjee, D., & Doyle, J. G. 2007, A&A, 475, L25
Parker, E. N. 1953, ApJ, 117, 431
Raftery, C. L., Gallagher, P. T., & Milligan, R. O. 2008, in ASP Conf. Ser. 397, First Results From Hinode, ed. S. A. Matthews, J. M. Davis, & L. K. Harra (San Francisco, CA: ASP), 184
Raftery, C. L., Gallagher, P. T., Milligan, R. O., & Klimchuk, J. A. 2009, A&A, 494, 1127
Reale, F. 2007, A&A, 471, 271
Reale, F. 2016, ApJL, 826, L20
Reale, F., & Landi, E. 2012, A&A, 543, A90
Reale, F., Landi, E., & Orlando, S. 2012, ApJ, 746, 18
Reeves, K. K., & Golub, L. 2011, ApJL, 727, L52
Rosner, R., Tucker, W. H., & Vaiana, G. S. 1978, ApJ, 220, 643
Ryan, D. F., Chamberlin, P. C., Milligan, R. O., & Gallagher, P. T. 2013, ApJ, 778, 68
Ryan, D. F., Milligan, R. O., Gallagher, P. T., et al. 2012, ApJS, 202, 11
Scharmer, G. B. 2006, A&A, 447, 1111

Scharmer, G. B., Bjelksjo, K., Korhonen, T. K., Lindberg, B., & Petterson, B. 2003a, Proc. SPIE, 4853, 341
Scharmer, G. B., Dettori, P. M., Lofdahl, M. G., & Shand, M. 2003b, Proc. SPIE, 4853, 370
Scharmer, G. B., Narayan, G., Hillberg, T., et al. 2008, ApJL, 689, L69
Schrijver, C. J. 2001, SoPh, 198, 325
Scullion, E., Rouppe van der Voort, L., Wedemeyer, S., & Antolin, P. 2014, ApJ, 797, 36
Susino, R., Lanzafame, A. C., Lanza, A. F., & Spadaro, D. 2010, ApJ, 709, 499
Sylwester, B., Sylwester, J., Serio, S., et al. 1993, A&A, 267, 586
Terzo, S., Reale, F., Miceli, M., et al. 2011, ApJ, 736, 111
Tihonov, A. N. 1963, Dokl. Akad. Nauk SSSR, 151, 501
Tripathi, D., Mason, H. E., Dwivedi, B. N., del Zanna, G., & Young, P. R. 2009, ApJ, 694, 1256
van Noort, M., Rouppe van der Voort, L., & Löfdahl, M. G. 2005, SoPh, 228, 191
Viall, N. M., & Klimchuk, J. A. 2012, ApJ, 753, 35
Vissers, G., & Rouppe van der Voort, L. 2012, ApJ, 750, 22
Warren, H. P. 2006, ApJ, 637, 522
Warren, H. P., Brooks, D. H., & Winebarger, A. R. 2011, ApJ, 734, 90
Warren, H. P., & Winebarger, A. R. 2007, ApJ, 666, 1245
Wilhelm, K., Lemaire, P., Curdt, W., et al. 1997, SoPh, 170, 75
Winebarger, A. R., Schmelz, J. T., Warren, H. P., Saar, S. H., & Kashyap, V. L. 2011, ApJ, 740, 2